

**EVOLUTIONARY GROUND REACTION FORCE CONTROL OF A  
PROSTHETIC LEG TESTING ROBOT**

**RONALD DAVIS**

**Bachelor of Electrical Engineering**

Cleveland State University

December, 2012

Submitted in partial fulfillment of the requirements for the degree of

**MASTER OF SCIENCE IN ELECTRICAL ENGINEERING**

At the

**CLEVELAND STATE UNIVERSITY**

August, 2013

**We hereby approve the thesis of**

**Ronald Davis**

**Candidate for the Master of Science in Electrical Engineering degree.**

**This thesis has been approved for the department of**

**ELECTRICAL AND COMPUTER ENGINEERING**

**and**

**CLEVELAND STATE UNIVERSITY**

**College of Graduate Studies by**

---

**Thesis Committee Chairperson, Dr. Dan Simon**

---

**Department & Date**

---

**Dr. Hanz Richter**

---

**Department & Date**

---

**Dr. Antonie van den Bogert**

---

**Department & Date**

---

**Dr. Eugenio Villaseca**

---

**Department & Date**

**Students Date of Defense: 12/11/2013**

## **ACKNOWLEDGMENTS**

I would like to thank my entire advising committee for all of their suggestions and help along the way of writing this thesis. Without them this thesis would have never been possible. I want to thank Dr. Simon for his guidance, support and numerous suggestions to improve the quality of this thesis. I want to thank Dr. Richter for the many hours we spent together in his office and lab working on the robot and related issues. I want to thank Dr. van den Bogert for always assisting me whenever I had a question related to biomechanics or human gait. I would like to thank Dr. Villaseca for exposing me to many of the concepts used in this thesis throughout all of his courses.

I would like to thank all of my fellow lab mates and students at CSU that helped me along the way. Special thanks goes to George Thomas for helping me with the simulation in this thesis.

I would last, but certainly not least, like to thank my family and friends who supported and believed in me throughout the writing of this thesis. I could not have done this without their constant love and support.

# **EVOLUTIONARY GROUND REACTION FORCE CONTROL OF A PROSTHETIC LEG TESTING ROBOT**

**RONALD DAVIS**

## **ABSTRACT**

Typical tests of prosthetic legs for transfemoral amputees prove to be cumbersome and tedious. These tests are burdened by acclimation time, lack of repeatability between subjects, and the use of complex gait analysis labs to collect data. To create a new method for prosthesis testing, we design and construct a robot that can simulate the motion of a human hip. We discuss the robot from concept to completion, including methods for modeling and control design. Two single-input-single-output (SISO) sliding mode controllers are developed using analytical and experimental methods. We use human gait data as reference inputs to the controller. When doing so we see the problems associated with the gait data that make it unfit for use as reference data. We apply a smoothing algorithm to correct the gait data. The robot is evaluated based on its ability to track the gait data. Despite proper tracking of the reference inputs, operating the robot with a passive prosthesis shows that the robot cannot adequately produce the ground reaction force (GRF) of an able bodied person. We devise a novel method to control GRF of the robot/prosthesis combination based on the way that human subjects walk with a prostheses. When walking with a prosthesis, users compensate for the deficiencies of the prosthesis by modifying their gait patterns. To simulate this we use an

evolutionary algorithm called biogeography-based optimization (BBO). We use BBO to modify the reference inputs of the robot, minimizing the error between the able-bodied GRF data and that of the robot walking with the passive prosthesis. Experimental results show a 62% decrease in the GRF error, effectively showing the robot's compensation for the prosthesis and improved control of GRF.

# TABLE OF CONTENTS

ACKNOWLEDGMENTS .....	iii
ABSTRACT.....	iv
LIST OF TABLES .....	ix
LIST OF FIGURES .....	x
ACRONYMS .....	xii
CHAPTERS	
I. INTRODUCTION.....	1
1.1 Overview.....	1
1.2 Literature Review.....	3
1.3 Contribution of Thesis .....	7
1.4 Organization of Thesis.....	7
II. CONSTRUCTION OF THE HIP ROBOT (HR).....	9
2.1 Overview.....	9
2.2 Components .....	11
2.3 Assembly and Electrical work .....	13
2.4 Modeling of Drive Stages .....	14
2.4.1 Analytical Derivation.....	15
2.4.2 Parameter Estimation.....	16
2.5 Simulink and dSpace.....	17
2.6 Ground Reaction Force (GRF) Measurement.....	19
III. SLIDING MODE CONTROL (SMC).....	21
3.1 Overview.....	22
3.2 Derivation of Sliding Mode .....	23
3.3 Hip Robot Input Trajectory Smoothing .....	24

3.3.1 Input Trajectory Optimization Derivation .....	25
3.3.2 Optimization Results.....	27
3.4 Implementation of Controller on Robot.....	29
3.5 Controller Tracking.....	31
IV. GROUND REACTION FORCE (GRF) CONTROL.....	36
4.1 Overview.....	36
4.2 Biogeography Based Optimization (BBO) .....	37
4.3 Application of BBO .....	39
4.4 Hip Robot (HR) Simulation .....	41
4.4.1 Simulation Characteristics .....	41
4.4.2 Simulation Results .....	44
4.5 BBO Application to HR.....	47
4.5.1 Phase 1: Bias BBO.....	50
4.5.2 Phase 2: Delta-Displacement BBO.....	53
V. CONCLUSION.....	57
5.1 Summary.....	57
5.2 Future Work.....	58
REFERENCES .....	60
APPENDICES .....	66
A: Wiring Lists and Schematics .....	67
Linear Motor: Main Power and Encoder .....	68
Rotary Motor: Main Power and Encoder.....	71
System: Servo On and Emergency Stop .....	73
System: Limit Switches .....	75
dSpace: Encoder and Control Signals.....	77
dSpace: Remaining Signals.....	79
B: Robot Simulink Diagram .....	82
Hip Robot Simulink Schematic: .....	82

Hip Robot Simulink Subsystems: ..... 84

C: dSpace ..... 86

    Instruments..... 86

    dSpace-HMI..... 88

## LIST OF TABLES

Table I: Linear drive-stage parameters. ....	12
Table II: Rotary drive-stage parameters. ....	13
Table III: Rotary drive-stage power supply parameters. ....	14
Table IV: Linear drive-stage model parameters. ....	17
Table V: Rotary drive-stage model parameters. ....	17
Table VI: SMC gains for linear and rotary drive-stage. ....	31
Table VII: HR Simulation BBO parameters. ....	44
Table VIII: HR Simulation BBO results. ....	45
Table IX: Bias BBO parameters. ....	51
Table X: Delta-displacement BBO. ....	54

## LIST OF FIGURES

Figure 1: System block diagram .....	2
Figure 2: Body planes .....	10
Figure 3: Hip robot schematic.....	11
Figure 4: Completed assembly of the HR, set up with a passive prosthesis.....	14
Figure 5: dSpace connection input/output board. ....	18
Figure 6: Forces and angles of the human/prosthetic leg combination .....	20
Figure 7: Original data and smoothed data .....	28
Figure 8: Vertical velocity vs. time.....	28
Figure 9: SMC as implemented in Simulink.....	29
Figure 10: Mauch Microlite S prosthesis with an Össur Flex Foot .....	32
Figure 11: Vertical displacement vs. time .....	33
Figure 12: Hip angle vs time.....	33
Figure 13: Knee angle vs. time .....	34
Figure 14: GRF vs. time.....	35
Figure 15: Immigration and emigration rates vs. number of species.....	38
Figure 16: Simulation flowchart. ....	43
Figure 17: Simulation vertical displacement vs. time.....	44
Figure 18: Simulation GRF vs. time.....	45
Figure 19: Simulation cost vs. generation.....	46
Figure 20: Simulated vertical displacement vs. time after BBO. ....	46
Figure 21: Simulated GRF vs. time after BBO.....	47

Figure 22: Flowchart of BBO process on HR.....	49
Figure 23: Cost vs. generation after phase 1 of BBO .....	52
Figure 24: Vertical displacement vs. time after phase 1 of BBO .....	52
Figure 25: Thigh angle vs. time after phase 1 of BBO .....	53
Figure 26: GRF vs. time after phase 1 of BBO.....	53
Figure 27: Cost vs. generation after phase 2 of BBO .....	55
Figure 28: Vertical displacement vs. time after phase 2 of BBO .....	56
Figure 29: GRF vs. time after phase 2 of BBO .....	56
Figure 30: Hip robot Simulink diagram (part 1/2).....	82
Figure 31: Hip robot Simulink diagram (part 2/2).....	83
Figure 32: "Trajectory Generation 1" Simulink subsystem.....	84
Figure 33: "Trajectory Generation 2" Simulink subsystem .....	85
Figure 34: Slider from dSpace. ....	86
Figure 35: Input box from dSpace. ....	86
Figure 36: Plotter in dSpace.....	87
Figure 37: Display from dSpace. ....	87
Figure 38: Selector button from dSpace. ....	87
Figure 39: dSpace HMI system (part 1/3).....	88
Figure 40: dSpace HMI system (part 2/3).....	90
Figure 41: dSpace HMI system (part 3/3).....	90

## ACRONYMS

<b>BBO</b>	Biogeography-Based Optimization
<b>CC</b>	Cleveland Clinic
<b>CSU</b>	Cleveland State University
<b>DOF</b>	Degrees of Freedom
<b>EE</b>	Electrical Engineering
<b>EMC</b>	Embedded MATLAB <sup>®</sup> Code
<b>GRF</b>	Ground Reaction Force
<b>HMI</b>	Human Machine Interface
<b>HR</b>	Hip Robot
<b>HSI</b>	Habitat Suitability Index
<b>ME</b>	Mechanical Engineering
<b>SISO</b>	Single Input Single Output
<b>SIV</b>	Suitability Index Variable
<b>SMC</b>	Sliding Mode Control

# **CHAPTER I**

## **INTRODUCTION**

### **1.1 Overview**

Cleveland State University (CSU) and the Cleveland Clinic (CC) have partnered to develop a new hydraulic prosthesis for above-knee (transfemoral) amputees [2], [39]. The proposed prosthetic leg features a unique semi-active design. The knee stores energy when the user puts weight on the leg and releases the stored energy as the knee straightens. Therefore the prosthesis has the ability to produce positive work at the knee, a feature not present in most prostheses [2].

To create an environment to test the new prosthesis, the partnership between CSU and CC also includes the design and construction of a robot that simulates the kinematics of a human hip. The hip robot (HR) will be used to test the new prosthesis and other prostheses such that comparisons can be made. Having a robot test platform provides a systematic approach to prosthesis testing, which often can be hazardous and lack

repeatability due to the use of human subjects [19]. The HR provides a safe testing environment with repeatability and no liability issues.

This thesis documents the design and construction of the HR, and also a novel approach to control the ground reaction force (GRF) produced by a prosthetic leg while being tested with the HR.

We begin in Section 1.2 with a literature review where we discuss problems due to the use of prostheses and the limitations of currently available prosthetic legs. We also discuss sliding mode control (SMC) and biogeography-based optimization (BBO). We use SMC on the HR for motion control. We use BBO to optimize the hip motions produced by the HR in order to obtain a desired GRF; a block diagram characterizing this can be seen in Figure 1. BBO monitors the GRF as read from a load cell. Based on the GRF reading, BBO modifies the input trajectory to alter the HR's movement. This produces different GRFs. SMC tracks the BBO modified trajectory. SMC accomplishes this using both position and velocity feedback.

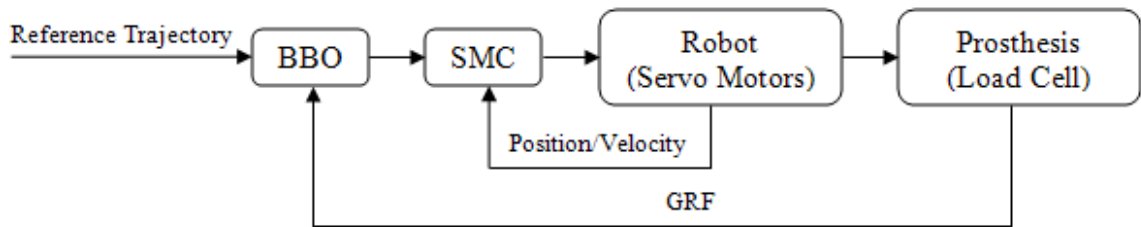


**Figure 1: System block diagram. BBO uses GRF feedback while SMC uses position and velocity feedback.**

In Section 1.3 we present the contribution of the thesis. Lastly, in Section 1.4 the organization of the thesis is presented.

## 1.2 Literature Review

Prosthetic legs for transfemoral amputees are known to produce negative side effects on their users [30]. Amputees alter their walking motions or gait dynamics to compensate for the deficiencies of their prosthesis. This can cause a user to exert up to 65% more energy than an able bodied person during normal walking [37]. This results in higher strains and loading on the intact limb, which eventually leads to secondary physical conditions such as osteoarthritis, osteoporosis, back pain, or joint pain [24], [30].

Secondary conditions can be due to a variety of issues, including improper alignment of the prosthesis, improper training for the use of the prosthesis, or a poor prosthetic-fit [30]. However, we can also attribute negative side effects to the fact that a majority of transfemoral prosthesis users wear a passive prosthetic knee.

We define a passive prosthetic knee as one that has no source of power and is a purely mechanical device with some form of damper. The damper typically has a spring-loaded design and the prosthesis dissipates energy [14]. Passive knees limit a user's gait. They do not vary their resistance during swing phase and they do not have the ability to self-actuate like a biological knee [13]. Because of this, prosthesis users develop gait deviations which result in the secondary physical conditions mentioned previously [30]. An in-depth look at amputee gait with passive prostheses can be found in [36].

A more advanced prosthesis type is the variable-damper. Here a microcontroller varies the damping or resistance of the prosthetic knee during the gait cycle to provide a gait cycle that is closer to that of an able-bodied person. Devices that utilize a variable damping knee are the Otto Bock C-Leg<sup>®</sup>, Össur Rheo Knee<sup>®</sup>, and the Endolite Adaptive Knee [25]. These designs yield promising results for users of transfemoral prostheses.

Variable-damping knees provide better gait stability than passive units. Unlike passive units, they allow the user to easily change gait speeds without adjustment. Users of variable-damping prostheses report less fatigue, easier locomotion, and more mobility than with a passive leg [3, 22, 24]. Unfortunately, these designs still lack the ability to deliver power at the knee, which impairs the user's ability to have a normal gait cycle [14].

Other prosthesis designs have elected to use an active knee. In this type of prosthesis an electric motor or hydraulic actuator powers the knee joint. Examples include the Össur Power Knee™ [2] or the Bionic Leg Prosthesis with actuated knee and ankle [12, 13, 14, 15]. The goal of these prostheses is to restore power to the knee so the user can walk with gait similar to an able bodied person. Results show that active knees do provide a gait cycle closer to those of able-bodied biomechanics. However, these prostheses have limited success because of their large power consumption compared to variable damping legs and are therefore limited in their application [2].

The biggest issue facing active knees is their power sources [14]. Using lithium-ion battery technology, the Bionic Leg Prosthesis can provide up to 9 km walking distance [15]. This distance is expected to double in the next five years as battery technology increases, potentially providing a prosthesis with 20 km of walking distance [15].

The hydraulic prosthesis in development at CSU blends a variable-damping and an active design, creating a unique semi-active knee. It consists of a hydraulic actuator, a closed hydraulic system, and two flow valves to regulate the control of hydraulic fluid. This design allows the prosthesis to store energy during stance-phase knee flexion. The

stored energy can be used to allow the user to perform movement when positive work is necessary [2]. The knee uses a closed hydraulic system so it is always pressurized. This means a pump is not required. The only power drawn is from the microcontroller and opening and closing of the valves. This results in a knee that draws similar power levels to a variable-damping knee, but includes the ability to produce positive work [38].

To develop the semi-active leg and verify its operation, an appropriate test routine must be created. Typical tests of transfemoral prostheses are cumbersome and involve vigorous routines with human subjects [20]. Tests require acclimation time so subjects can become comfortable with the new prosthesis. This period of time can be up to three months [3]. Often these tests require the use of a safety harness to prevent falling. Tests require a gait or motion analysis lab where cameras, force plates, and other methods are used to collect kinetic and kinematic data of the prosthetic test [2, 3, 22, 24, 25]. These tests are not repeatable due to the often changing nature of human gait dynamics, which can be affected by factors such as height, weight, sex, fatigue, general health, or mood [17].

Due to the difficulties in testing prostheses, we design and construct a robot that can test transfemoral prostheses under various walking conditions. Using a robot for testing eliminates many of the factors present when testing with human subjects, making testing easier. By using a robot, liability and risk of danger are virtually nonexistent. Unlike humans, robots can operate continually without fatigue. Operation is continuous and prostheses can be tested under repeatable conditions. Testing with robotics eliminates the need for complex gait labs. The robot and prosthesis can be fitted with encoders, load

cells, and other sensors to measure quantities that are otherwise difficult to measure with human subjects [20].

The HR project combines efforts from both the mechanical engineering (ME) and the electrical engineering (EE) departments at CSU. We discuss construction and design of the HR later in this thesis. To mimic the movement of a human hip, the HR uses clinical human gait data as tracking inputs. We use SMC on the drive-stages of the HR for feedback control.

SMC has been proven in the aerospace industry, robotics, power electronics, and more. We choose SMC due to its popularity, ease of application, robustness, and disturbance rejection properties [19]. In [23] SMC was used to control the flight of a four-rotor mini flying robot. In [26] a two wheeled robot was controlled using SMC to maintain the robot upright like an inverted pendulum. SMC will be shown in this thesis to yield good tracking of the robot motion profiles.

Besides input tracking, we also test GRF control with the HR. When testing the robot with able-bodied gait data, GRF of the robot did not match able-bodied GRF from the human gait data. During these tests the drive-stages of the robot exhibited good input tracking performance. We accept poor GRF tracking because we are using a passive knee to simulate able-bodied walking. However, it is of interest to see if the HR could walk with a GRF to match the able-bodied data. Doing so would require the robot to compensate for the prosthesis, much like a human user would. To simulate human compensation for a prosthesis and control the GRF of the HR, we modify the input trajectories of the HR, indirectly controlling the GRF. BBO optimizes the input reference trajectory so the desired GRF is obtained.

BBO is a recently developed evolutionary algorithm (EA). It has been shown to perform better on many benchmark functions than traditional EAs, and has been applied successfully to many real world optimization problems [6]. BBO has previously been used to optimize the controls of CSU's semi-active knee with initial simulation results documented in [18, 38, 39]. For a more in-depth look at BBO, see Chapter 4.

### **1.3 Contribution of Thesis**

This thesis documents the design, development, and construction of the HR. Modeling techniques for drive stages of the robot and design of the controllers for those respective systems are investigated. We evaluate human gait cycle data and show characteristics which make it unfit to be a reference trajectory for the HR. To adjust the data, we apply an algebraic spline interpolation method to smooth the data and solve the problems with the raw data. The performance of the robot is evaluated based on its ability to follow these optimized reference trajectories. Lastly we show that BBO can modify the able-bodied gait data such that the robot walks with a desired GRF.

### **1.4 Organization of Thesis**

Chapter 2 discusses the building of the robot. We look at the construction of the robot, investigate the modeling of the robot, determine control parameters, and also discuss implementation of the controllers.

Chapter 3 investigates the design of the SMC. We look at the theoretical derivation of SMC. We present the limitations of human gait cycle data as useable reference inputs to the HR. We then apply a smoothing optimization algorithm to make

the data usable as reference inputs to the HR. We lastly evaluate the performance of the robot in following the smoothed reference trajectories.

Chapter 4 describes the method used for GRF control. We present BBO and how it works. We then apply it to the HR to modify the input trajectories and obtain a desired GRF. We end the chapter by examining the experimental results.

In Chapter 5 we conclude this thesis. We summarize the main ideas of the thesis and the results from the experiments. As a final remark we look at ideas for future work.

## **CHAPTER II**

### **CONSTRUCTION OF THE HIP ROBOT (HR)**

We begin by discussing the design, construction, and modeling of the HR. In Section 2.1, the basics of the design are presented. This discussion includes the desired operation and motion of the HR. Section 2.2 documents the technical aspects of the HR. Here we look at the physical components used to construct the HR. In Section 2.3 we look at the electrical system of the robot. Section 2.4 presents the mathematical modeling of the HR's drive-stages. Shown also are the experiments used to determine the parameters for those models. Lastly, in Section 2.5, we discuss the software and hardware used to operate the robot.

#### **2.1 Overview**

Construction of the robot was a joint effort between the ME and EE departments at CSU. The ME department designed the frame of the robot and found components that would meet the desired specifications for the drive stages. Another account of the HR work can be found in [20]. The research conducted as part of this thesis includes the

wiring and integration of the motors, drivers, and computer software into one functioning unit.

Robot operation imitates the motion of a human hip during gait. We limit motion to two degrees of freedom (DOF): vertical hip displacement and thigh angle parallel to forward motion or in the sagittal plane. The planes of the body are shown in Figure 2. We do not allow thigh movement perpendicular to forward motion, or in the coronal plane, for the sake of simplicity and because we only wish to emulate straight-line walking at this time.

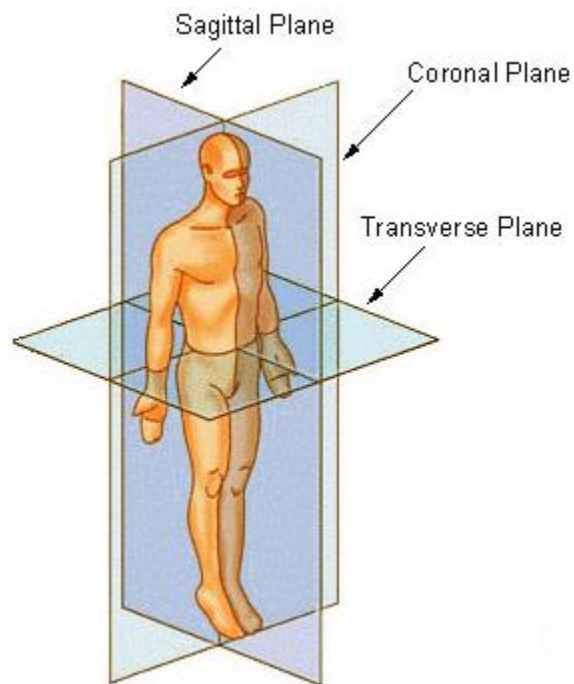


**Figure 2: Body planes. The HR only allows for motion in the sagittal plane.  
Picture used under the Wikipedia Commons free license.**

Human gait cycle data was obtained from the CC [2]. We use this data as reference inputs for tracking to both drive stages of the HR. The machine consists of four main components: the frame, treadmill, linear drive-stage, and rotary drive-stage. Both drive-stages were modeled for ease of control development and simulation. To implement

control of the drive stages and all other operating functions of the robot, Simulink<sup>®</sup> and dSpace<sup>®</sup> software and hardware are used.

## 2.2 Electrical and Mechanical Components

The frame was designed so that it can withstand forces generated by the actuation of the drive stages and prosthesis. Nuts, bolts, and fasteners were selected to meet those criteria as well. The frame is constructed of welded A500 rectangular steel tubing using bolts to attach mounting plates for drive-stages and the treadmill. All joints were verified for static loading and fatigue using SolidWorks<sup>®</sup> software. Component life was also estimated at this time. The treadmill is bolted to the base of the frame to establish a walking platform for any prosthesis tested. A schematic of the robot design is shown in Figure 3.

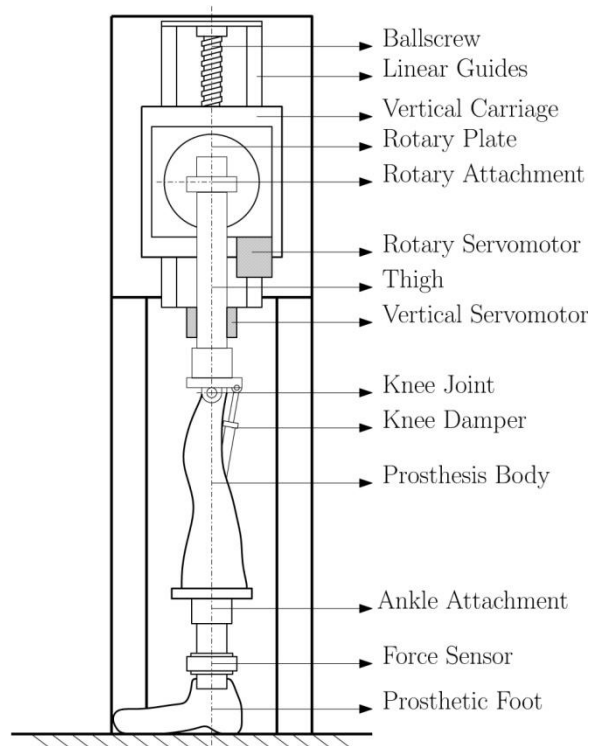


Figure 3: Hip robot schematic [20].

The linear drive-stage consists of a brushless DC servo-motor, servo amplifier, and ballscrew-driven linear slide. We configure the servo amplifier to run in torque mode so the analog input voltage is theoretically proportional to the output torque of the motor. The ballscrew mounts vertically to the robot frame to provide variation of vertical hip displacement. The ballscrew has 12 inches of travel but on average we use only 100 mm of travel for different motion profiles. We use the remaining distance to adjust the center of oscillation so shorter or longer prostheses can be tested. An incremental encoder attached to the servo motor measures both position and velocity. Absolute position of the ballscrew is achieved using a limit switch on the top end of travel of the linear slide.

Table I shows the parameters of the drive stage.

<b>Linear Drive-Stage</b>		
<b>Servo Amplifier</b>	<i>Manufacturer</i>	Mitsubishi
	<i>Model No.</i>	MR-J3-70A
	<i>Configuration</i>	Torque Mode
<b>Servo Motor</b>	<i>Manufacturer</i>	Mitsubishi
	<i>Model No.</i>	HF-KP73
	<i>Rated / Max Speed</i>	3000 / 6000 RPM
	<i>Torque Rated / Max</i>	7.2 / 8.36 Nm
	<i>Inertia Moment</i>	1.43E-4 J-Kg-m <sup>2</sup>
	<i>Current Rated / Max</i>	5.2 / 15.6 A
<b>Linear Slide</b>	<i>Manufacturer</i>	RAF Automation
	<i>Usable Travel</i>	12 in
	<i>Lead</i>	0.5 in / revolution

**Table I: Linear drive-stage parameters.**

The rotary drive-stage also contains a brushless DC servo-motor and servo amplifier. The motor drives a rotary-stage via a direct coupling and an inchworm-gear reducer. Like the linear drive-stage, the servo amplifier is also configured for torque mode. The entire rotary stage attaches to the linear slide's carriage, so the entire rotary drive-stage moves vertically when varying vertical hip displacement. When operating we establish absolute position of the rotary stage with a limit switch. Angular position and

angular velocity are measured using an incremental encoder. Table II lists the parameters of the rotary drive stage.

<b>Rotary Drive-Stage</b>		
<b>Servo Amplifier</b>	<i>Manufacturer</i>	Electrocraft
	<i>Model No.</i>	SA-B4-70-10
	<i>Configuration</i>	Torque Mode
<b>Servo Motor</b>	<i>Manufacturer</i>	Electrocraft
	<i>Model No.</i>	RapidPower RP34
	<i>Rated/Max Speed</i>	1800/2250 RPM
	<i>Torque Rated / Max</i>	2.21 / 7.73 N-m
	<i>Rotor Inertia</i>	2718.9 gm-cm <sup>2</sup>
	<i>Current Rated / Max</i>	22.7 / 79.3 A
<b>Stage</b>	<i>Manufacturer</i>	Newmark Systems
	<i>Usable Travel</i>	360°
	<i>Drive Ratio</i>	80:1
	<i>Max Torque</i>	75 N-m (Measured)

**Table II: Rotary drive-stage parameters.**

### 2.3 Assembly and Electrical Work

Assembly and wiring of the robot was completed in the Robotics and Mechatronics lab at CSU. All fasteners were tightened to design specifications using a calibrated torque wrench. Wiring sizes and types also meet manufacturer suggested criteria. Linear-stage servo amplifier power comes from a wall mounted 220 V line. Rotary-stage power comes from a power source that runs on a standard 110 V power outlet. Specifications of the rotary-stage power supply are shown in Table III. Wiring schematics and lists for the entire HR can be found in Appendix A. Figure 4 shows a picture of the completed assembly of the robot.

<b>Rotary Drive-Stage Power Supply</b>	
<i>Manufacturer</i>	Ascom Frako
<i>Model No.</i>	E24/8 WRGD-E77-527-2300
<i>Input Power</i>	3.3 A at 110 - 120 VAC
<i>Output Power 1</i>	8 A at 24 VDC
<i>Output Power 2</i>	3 A at 5 VDC

**Table III: Rotary drive-stage power supply parameters.**



**Figure 4: Completed assembly of the HR, set up with a passive prosthesis [20].**

## **2.4 Modeling of Drive Stages**

Modeling was completed as a joint effort between the EE and ME departments. The work discussed in this section is based on [20] and is included here for the sake of completeness.

To model the various features of the HR, many methods were used, including analytical derivations, set-point tests, load tests, and chirp signal tests. The analytical derivations provide the structure of each drive-stage model. We then test each drive-stage

to find values for variables within those model structures. Since both stages are configured to run in torque mode we can model them as current driven DC machines with inertias:

$$\tau = J\ddot{\theta} = ik \quad (2.1)$$

where  $\tau$  represents torque of the motor,  $J$  the total inertia of the stage,  $\ddot{\theta}$  angular acceleration,  $i$  the input current, and  $k$  the torque constant of the motor.

#### 2.4.1 Analytical Derivation

For the vertical stage we ignore viscous damping and concern ourselves with friction of the carriage on the guides. This provides the following ballscrew torque balance equation:

$$\tau_{m1} - \tau_c = J\ddot{\theta} \quad (2.2)$$

where  $\tau_m$  represents motor torque and  $\tau_c$  represents torque due to the reaction of the carriage on the screw. We also know that a ballscrew with lead  $l$  and efficiency  $\eta$  has thrust force  $F$ :

$$F = \frac{\tau_c}{l} 2\pi\eta \quad (2.3)$$

We define motor torque  $\tau_{m1}$  as follows:

$$\tau_{m1} = \frac{k_1 u_1 l}{2\pi\eta} \quad (2.4)$$

where  $k_1$  relates input voltage of the servo amplifier to output torque, and  $u_1$  is the input voltage. Combining Equations 2.2, 2.3, and 2.4 gives the total thrust force that the motor delivers to the carriage:

$$F = k_1 u_1 - \frac{2\pi\eta J\ddot{\theta}}{l} \quad (2.5)$$

The rotary-stage can be modeled more simply using the basic model for a DC current driven machine. We consider viscous damping due to the drivetrain and account for the internal gear ratio (80:1) of the drive-stage. We take the Laplace transform of Equation 2.1 and include the viscous damping coefficient  $b$ :

$$\dot{\theta}(s) = \frac{u_2(s)k_2}{(J_0 + n^2J_m)s + b} \quad (2.6)$$

where  $u_2$  represents the input voltage,  $k_2$  a constant which relates input voltage of the servo amplifier to output torque,  $J_0$  the inertia of the rotary stage actuator gear,  $n$  the gear ratio, and  $J_m$  the inertia of the worm gear and motor armature.

#### 2.4.2 Parameter Estimation

Each drive stage was operated through various tests to experimentally determine the unknown variables in the modeling equations. For the linear drive-stage, a series of set point tests were performed to determine  $k_1$ . In these tests the slide's carriage was placed against a load cell to measure force, input voltages  $u_1$  were then applied, and the resultant forces were recorded. We used linear regression to determine the value for  $k_1$ .

To determine  $\frac{l}{2\pi\eta}$ , as given in Equation 2.3, the carriage was statically pressed against a load cell. Thrust and torque were measured using a torque cell. Those values were used in a linear regression equation to determine a value for  $\frac{l}{2\pi\eta}$ . Using back calculation, a value for efficiency  $\eta$  was also found. Using the same torque cell, we found braking torque of the carriage due to friction on the slides. The final values for the model are shown in Table IV.

Parameter	Value
$k_1$	375 N / V
$\eta$	0.84
$J$	0.0015 kg-m <sup>2</sup>
$l / (2\pi\eta)$	0.0024 m / rad

**Table IV: Linear drive-stage model parameters.**

A swept-sinewave signal was applied as the input voltage to determine the unknowns for the rotary stage. Using the MATLAB System Identification Toolbox™, a transfer function was derived using the input and output information from the swept-sinewave test. Since this only provides us with values of the ratios  $k_2/(J_0 + n^2J_m)$  and  $k_2/b$ , we then experimentally determined values for  $k_2$  by attaching a bar to the rotary stage, and driving the bar into a load cell. Step inputs were applied and the resulting force measured. We used linear regression to determine the value for  $k_2$ . With  $k_2$  we could find values for  $J_0$  and  $b$  since the motor's spec-sheet contains  $J_m$ . Final values for the rotary stage model are shown in Table V.

Parameter	Value
$k_2$	15 N-m / V
$J_m$	1.82E-4 kg-m <sup>2</sup>
$J_o$	0.3352 kg-m <sup>2</sup>
$b$	9.75 N-m / s

**Table V: Rotary drive-stage model parameters.**

## 2.5 Simulink and dSpace

dSpace software and hardware, in conjunction with MATLAB Simulink, are used to provide feedback control and to develop a human machine interface (HMI) for the robot. Simulink uses a graphical programming interface to code the controllers and functions needed for HR operation. dSpace software provides an HMI where we can monitor and change signals coming from, and going to, the robot. It also includes the

hardware necessary to do so, including an internal computer processor and external connection board.

In the Simulink environment functions are displayed as blocks and the lines connecting the blocks represent the signal paths. dSpace software provides blocks within the Simulink environment that allow us to read various signals from the robot, and also to export signals to the robot. These signals can be analog or digital and are read and sent using the dSpace connection board shown in Figure 5. The Simulink model developed for the robot is shown in Appendix B. We use the Simulink/dSpace combination rather than an embedded processor due to ease of use and the simplicity to build dynamic functions without having to learn custom computer languages. Simulink also supports the Embedded MATLAB® coding language, a subset of the MATLAB language.

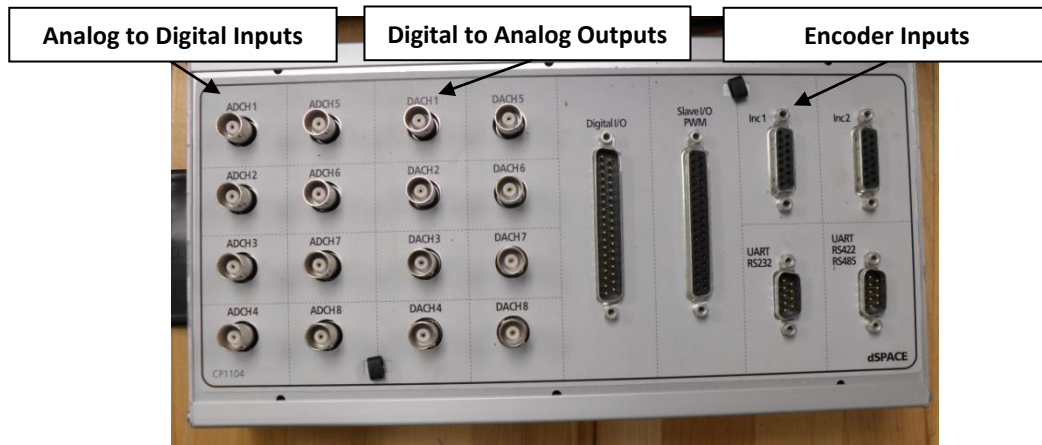


**Figure 5: dSpace connection input/output board.**

We use embedded MATLAB code (EMC) to implement many of the robot functions, safety triggers, and different modes of operation. EMC allows us to program functions that would be otherwise difficult to design using the typical block and line method in Simulink. The EMC language is also used extensively in Chapter 4 of this thesis to implement BBO in the Simulink environment.

We use dSpace software to create the HMI for the robot. The software actively communicates with the Simulink model. This allows us to display and adjust values within the Simulink model in real time. Some of the basic dSpace operators that we use, such as the slider, input box, plotter, display, and selector button, are discussed in Appendix C. The complete HR dSpace HMI used for this thesis can also be found in Appendix C.

## 2.6 Ground Reaction Force (GRF) Measurement

When testing the HR, GRF is measured with a load cell attached to the prosthetic leg. Using a custom bracket, the load cell mounts between the prosthetic knee and foot. This is shown in Figures 3 and 10. Positioning the load cell at that location does not read GRF directly but measures force along the lower shank of the prosthesis. For GRF optimization, the measured force along the lower shank needs to be compared to the force from the reference gait data. The force along the lower shank is not provided in the gait cycle data; however, the three-dimensional decomposition of GRF is provided.

Using the combination of forces shown below, and visualized in Figure 6, force along the lower shank for the reference data was calculated:

$$F_a = F_x \cos \theta + F_y \sin \theta \quad (2.7)$$

where  $F_a$  is the force along the lower shank,  $F_x$  the forward component of GRF,  $F_y$  the vertical component of GRF, and  $\theta$  the angle of the lower shank.  $\theta$  is calculated from thigh angle  $h$  and knee angle  $k$  as follows:

$$\theta = h - k + \frac{\pi}{2} \quad (2.8)$$

For simplicity, and because  $F_a$  was calculated from reference GRF data,  $F_a$  will be referred to as GRF for the remainder of this thesis.

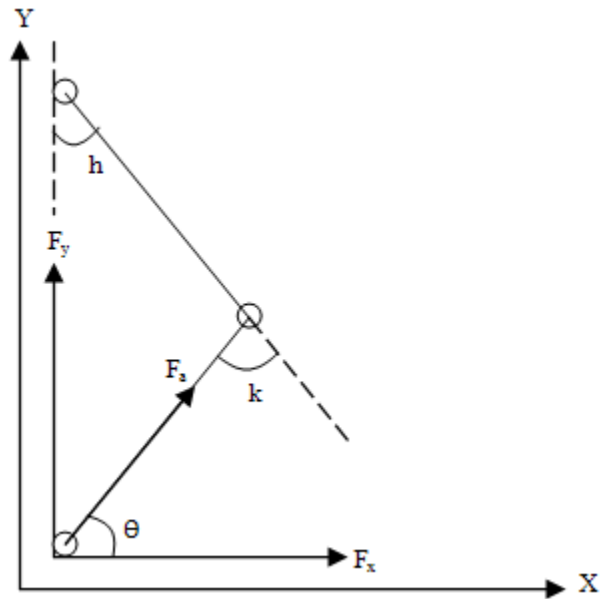


Figure 6: Forces and angles of the human/prosthetic leg combination:  $h$  = thigh angle,  $k$  = knee angle,  $\theta$  = shank angle, and  $F_a$  = shank force.

## **CHAPTER III**

### **SLIDING MODE CONTROL (SMC)**

In this chapter we present the design, implementation, and performance of the control system used for HR operation. We begin in Section 3.1 with a general overview of SMC. We discuss why we use SMC, and some of its drawbacks. Section 3.2 presents the mathematical derivation of a version of SMC applicable to the actuator models. Section 3.3 investigates the problems associated with using human gait data as tracking references to the HR. We address those problems by adjusting the gait cycle data using an optimization algorithm. In Section 3.4 we implement the controller on the HR. We present the use of Simulink, dSpace, and real time tuning methods for the controller. Section 3.5 presents the operation of the robot, where the HR is fitted with a prosthesis and tested. Lastly we examine the tracking of the robot compared to the reference motion profiles and analyze the performance of both controller and HR.

### 3.1 Overview

For control purposes we treat the robot as two independent closed loop single input single output (SISO) systems. The mechanical configuration of the robot allows us to do so by ignoring the forces generated between drive-stages. We assume the rotary drive-stages high gear ratio makes it non-back-drivable. For the vertical stage we assume that swinging the leg with the rotary stage will produce only small inertial changes that affect the linear stage [20].

We choose sliding mode control (SMC) due to its straightforward application and robustness properties [19]. SMC was developed in the late 1950's in the former Soviet Union by professors V. I. Utkin and S. V. Emelyanov [41]. It is a nonlinear control technique in which invariance properties guarantee disturbance rejection and robustness under some conditions.

Unlike a PID or similar controller, SMC does not require real-time integration or differentiation, which makes computer processing less of a burden. SMC is a switching algorithm and therefore susceptible to chattering [19]. It requires three inputs: the reference signal to be tracked, the reference signal's first derivative, and the reference signal's second derivative. When computing these derivatives, SMC requires smoothness of the signal and its derivatives. In most cases these derivatives are calculated off-line in order to avoid the need for real time differentiation of the input trajectory.

### 3.2 Derivation of Sliding Mode Control

In SMC we define a sliding manifold towards which we drive the system. For our purposes we follow the derivation of a basic SISO SMC which can be found in [19]. For a SISO system with desired response  $r$  and output  $y$  the error  $e$  is defined as:

$$e = r - y \quad (3.1)$$

We then define  $s$  as the sliding function:

$$s = \dot{e} + \lambda e \quad (3.2)$$

where  $\lambda > 0$  represents a constant tuning parameter of the controller. Introducing  $\dot{e}$  requires reference data  $\dot{r}$  and feedback  $\dot{y}$ . When the system is driven to the sliding function,  $s = 0$  and consequently  $\dot{e} = e = 0$ . To accomplish this we constrain the derivative of  $s$  to the signum function times a constant tuning parameter  $\eta > 0$ :

$$\dot{s} = -\eta \operatorname{sgn}(s) \quad (3.3)$$

This guarantees that as time increases,  $s$  goes to zero in some finite amount of time.

When  $s = 0$  the sliding function is reached. Taking the derivative of Equation 3.2 gives:

$$\dot{s} = \ddot{e} + \lambda \dot{e} \quad (3.4)$$

Substituting for  $\dot{s}$ ,  $\ddot{e}$ , and  $\dot{e}$ , we get:

$$\ddot{r} - \ddot{y} + \lambda(\dot{r} - \dot{y}) = -\eta \operatorname{sgn}(s) \quad (3.5)$$

This will be used later to derive our control signal  $u$ . Our drive-stages can be modeled as DC current-driven machines with damping:

$$\frac{y(s)}{u(s)} = \frac{k}{s(Js + b)} \quad (3.6)$$

where  $u$  is the control signal,  $k$  the combination servo amplifier gain and motor torque,  $J$  the inertia in the system, and  $b$  the viscous damping. Simplifying Equation 3.6, taking derivatives where necessary, and accounting for unknown torque disturbance  $\tau_d$  gives:

$$J\ddot{y} + \dot{y}b = ku + \tau_d \quad (3.7)$$

The torque disturbance  $\tau_d$  is ignored when deriving the control law. As shown in [20], its effects can be entirely rejected by choosing a sufficiently large  $\eta$ , provided the disturbance is bounded by a known constant. Solving (3.7) for  $\ddot{y}$  and substituting into Equation 3.5 yields:

$$\ddot{r} - \lambda\dot{r} - \lambda\dot{y} - \frac{k}{J}u + \frac{b}{J}\dot{y} = -\eta \operatorname{sgn}(s) \quad (3.8)$$

Solving for  $u$  we get the resultant control signal:

$$u = \frac{J}{k} \left[ \ddot{r} + \lambda\dot{r} + \left( \frac{b}{J} - \lambda \right) \dot{y} + \eta \operatorname{sgn}(s) \right] \quad (3.9)$$

Note in Equation 3.4 that  $s = \dot{e} + \lambda e$ . Therefore we need to calculate  $e$  and  $\dot{e}$ , which means our controller also requires output  $y$  and inputs  $r$  and  $\dot{r}$ . From the motor encoders we have feedback for position and velocity, or  $y$  and  $\dot{y}$ . To achieve SMC we need reference data  $r, \dot{r}$ , and  $\ddot{r}$ . Because of this, the input signal must be twice differentiable. Due to differentiability, it is also continuous. Since  $r$  is the reference trajectory, these derivatives can be calculated off-line or before they are used as inputs to the system to avoid the need for real-time differentiation.

### 3.3 Hip Robot Reference Input Trajectory Smoothing

Clinical human gait data for thigh angle and vertical hip displacement are used as inputs to the robot to emulate human hip motion. The CC provided the gait cycle data, which has limitations. Because of measuring methods, the data is only one stride or period in length. If the robot needs to operate for more than one stride, the data needs to be repeated cyclically. However, the data does not end at a point close to the start point. Because of this, when it is repeated, noise appears in the first derivative, and

consequently in the second derivative as well. Since SMC requires smoothness of the signal and its first two derivatives, we must adjust the input data to avoid those issues. In order to do this we smooth the data using an optimization algorithm.

### **3.3.1 Reference Input Trajectory Optimization**

Optimization provides a straightforward way to smooth the reference data. The reference input trajectories must satisfy two criteria. First, they must be defined within the three-dimensional space that the robot can move. Second, position, velocity, and acceleration must be continuous [35]. Generally we optimize the trajectory in between data points in order to minimize negative effects on the robot [9]. For our purpose, we have the predetermined clinical data that consists of many points that the robot must follow.

We can represent the gait cycle data using either a single polynomial or multiple polynomials splined together between concurrent data points. Using a single polynomial results in an extremely high order trajectory [34]. When constraining derivatives for smoothness the order is even higher [35]. Therefore we spline together multiple low order polynomials between adjacent data points to reduce the order and computational load of the trajectory [34]. We perform optimization using algebraic spline interpolation, and minimize the sum of squared error between the original data and the spline at the data points. Algebraic spline interpolation is used due to its popularity, simplicity, and ease of use [9]. We constrain the data in order to maintain the integrity of the original signal, resulting in a smoothed signal that closely resembles the original.

Algebraic spline interpolation represents the signal between each pair of data points using a polynomial. For the hip robot we require continuity of the input signal,

first derivative, and second derivative. For that reason we use a third order polynomial between each pair of data points [4]. Typically a higher order polynomial will be more likely to contain unnecessary oscillations [9]. We define our polynomial between two adjacent data point as follows:

$$f_i(t) = a_{i0} + a_{i1}t + a_{i2}t^2 + a_{i3}t^3 \quad (3.10)$$

where the  $a$  terms represent the polynomial coefficients. The interpolated signal is therefore:

$$f(t) = f_i(t) \quad (3.11)$$

where  $t \in [t_{i-1}, t_i]$ , and  $i \in [1, n - 1]$ , where  $n$  is the total number of data points in the clinically provided human gait data. This yields a family of  $n - 1$  polynomial functions, each with four  $a$  coefficients to represent the smoothed signal.

The algebraic spline method allows us to impose multiple constraints to adapt the optimization objective to our specific needs. For our purpose we want the data trajectory to be continuous and end at the same point as it starts, allowing us to repeat the gait cycle without discontinuities. We impose constraints for continuity:

$$f_i(t_i) = f_{i+1}(t_i) \quad (3.12)$$

$$f'_i(t_i) = f'_{i+1}(t_i)$$

$$f''_i(t_i) = f''_{i+1}(t_i)$$

for  $i \in [1, n - 2]$  and constraints for the start and end points:

$$f(0) = f(T) \quad (3.13)$$

$$f'(0) = f'(T)$$

$$f''(0) = f''(T)$$

where  $T = t_{n-1}$  is the time at the end of the gait cycle.

Using the constraints from (3.12) and (3.13), we use MATLAB function *quadprog* to implement the algebraic spline optimization. We minimize the sum of squared error defined as:

$$\sum_{i=0}^{n-1} (f(t_i) - f_i)^2 \quad (3.14)$$

where  $f(t_i)$  is the smoothed spline signal at time  $t_i$ , and  $f_i$  is the original data at index  $i$ . We optimize this subject to the  $3(n - 1)$  constraint equations in (3.12) and (3.13). Since we have a third order representation of the signal, with  $n$  data points, we optimize to find  $4(n - 1)$  unknowns.

### 3.3.2 Optimization Results

Results are shown in Figures 7 and 8. Figure 7 compares the original data and the smoothed data. We add one additional knot to the spline to aid the smoothing algorithm. As constrained, the next point after the end point of the smoothed data will be the start point of the next period of the smoothed data. This guarantees continuity between repetitions of the gait cycle data. Figure 6 shows the third order algebraic spline, maintaining the integrity of the original signal. Note that the original data is not periodic, but the spline is periodic.

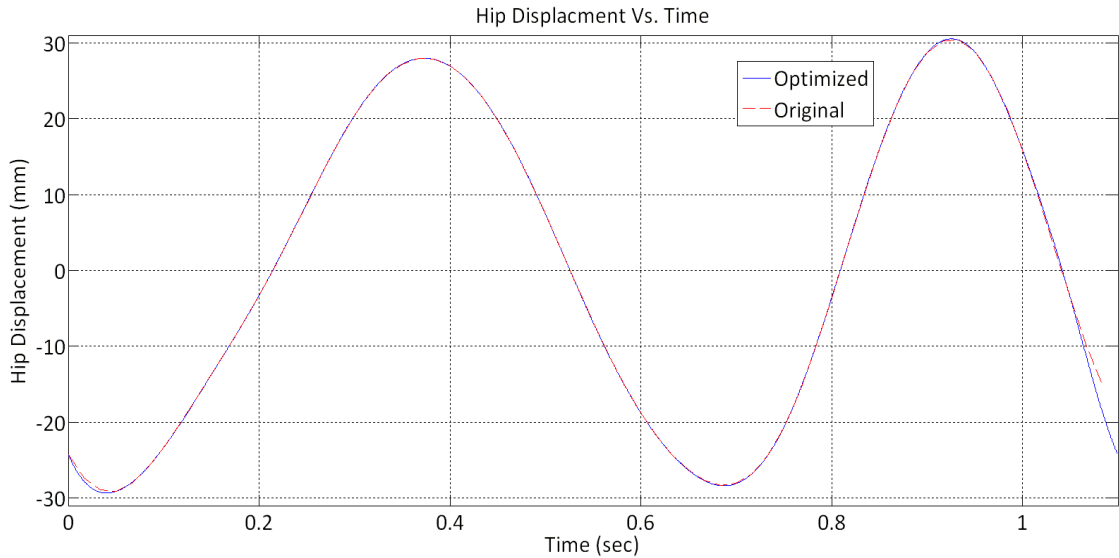


**Figure 7: Original data and smoothed data. The smoothed data has one additional knot and also ends such that the next point in a continuous cycle will be the first data point of the same cycle repeated.**

Figure 7 shows a comparison of the first derivative of the original data and the smoothed data. As intended, the smoothed data derivative is continuous, although the original data contains a discontinuous derivative between the gait cycle periods.

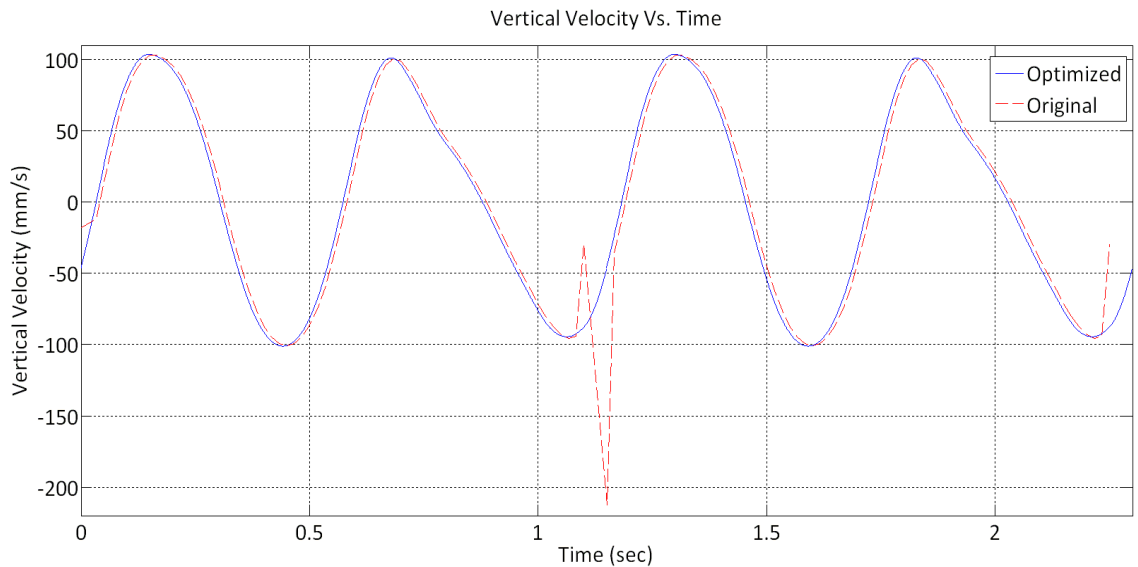


**Figure 8: Vertical velocity vs. time. The original data contains a discontinuity between gait cycle periods.**

### 3.4 Implementation of the Robot Controller

The controllers are implemented in the Simulink environment as shown in Figure 8. Notice that we approximate the signum function using a bounded saturation block and additional gain  $1/\Phi$ . This is done so that we can attenuate chattering in the control signal. We approximate the vertical slope of the signum function using the variable  $\Phi$ , which becomes the final tuning parameter of the controller.

The overall Simulink diagram of the robot system can be found in Appendix B. We use EMC blocks to implement the various functions of the robot and to incorporate some of the necessary safety features. We have four main modes of operation for the robot as noted previously in Section 2.5. The Simulink diagram consists of two main diagrams, one for each drive-stage. Those diagrams each consist of a signal input, controller, system output selector, and the controller output. We also have encoder readout blocks, as well as various inputs and outputs for the sensors that we wish to monitor during tests. Those sensors include: knee angle as measured by a potentiometer, GRF as measured by a load cell, and a safety trigger which monitors a force plate. The force plate contains four load cells that can detect hyper extension torque in the knee or excessive loading.

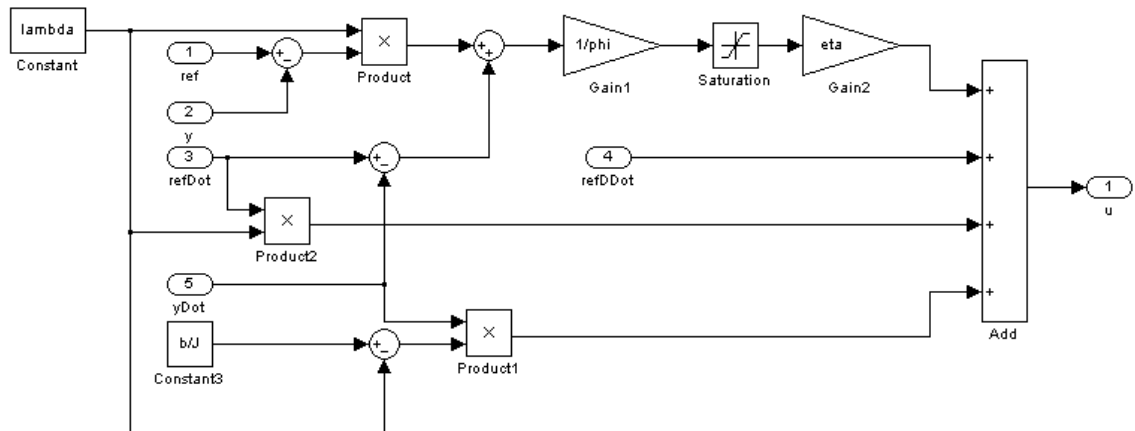


Figure 9: SMC as implemented in Simulink.

There are multiple safety triggers to prevent damage to the robot and ensure operator safety. There are limit switches to indicate if the robot has traveled outside of its safe operating range. We have a user controlled emergency stop button which immediately deactivates all robot functions. Velocity and acceleration limits are programmed into the servo amplifiers. Saturation blocks in the Simulink diagram prevent any analog signals from going outside of their safe operating ranges. Finally, a rate transition block prevents the vertical displacement reference from changing too quickly. The robot operator monitors GRF and deactivates the robot if unsafe readings are measured.

Tuning of the controller was performed in real time with dSpace. Since dSpace allows the manipulation of variables in real time, we configured dSpace sliders for each tuning parameter of the SMCs. The stages were run and the sliders adjusted until proper tracking was obtained. Adjusting  $\Phi$  allowed us to control the approximation of the signum function and attenuated chattering of the system. Adjusting  $\eta$  varied the switching gain of the system. Generally the higher  $\eta$  is, the less susceptible to disturbances the system became, but increases in  $\eta$  also increased chattering. Modifying  $\lambda$  adjusted the convergence speed of the error to the sliding manifold. The values for  $\eta$  and  $\lambda$  are extremely robust and have a wide range in which the robot operation is acceptable. The system is most sensitive to the adjustment of  $\Phi$  since this is the assumed slope we use for the signum function and has an immediate effect on chatter. The final control gains for both linear and rotary drive-stages are shown in Table VI.

<b>Control Parameters</b>		
<b>Linear Drive-Stage</b>	$\eta$	10000 (unitless)
	$\lambda$	9010 s <sup>-1</sup>
	$\phi$	166 s
<b>Rotary Drive-Stage</b>	$\eta$	50 (unitless)
	$\lambda$	10 s <sup>-1</sup>
	$\phi$	0.5 s

**Table VI: SMC gains for linear and rotary drive-stage.**

### 3.5 Controller Tracking

Each drive stage was run independently to verify proper operation. All safety features were validated at this time as well. After validation of proper operation and safety triggers, the HR was fitted with a passive prosthesis and both drive stages were run together.

We use standard prosthetic knee and foot components to test the robot. Both components are older models of currently available prostheses and therefore do not have specification data readily available. We use an Össur Mauch<sup>®</sup> Microlite S leg [43]. The Microlite S was chosen due to availability and because it is a standard passive knee design. This prosthesis utilizes two settings for its mechanical damper: a setting for flexion and a setting for extension of the knee. We configured the knee prosthesis with an Össur Flex-Foot<sup>®</sup> [42]. The Flex-Foot was chosen because it is a widely used prosthetic foot. A custom bracket was designed to fit a load cell between the prosthetic knee and foot. A photo of the assembled leg can be seen in Figure 9.

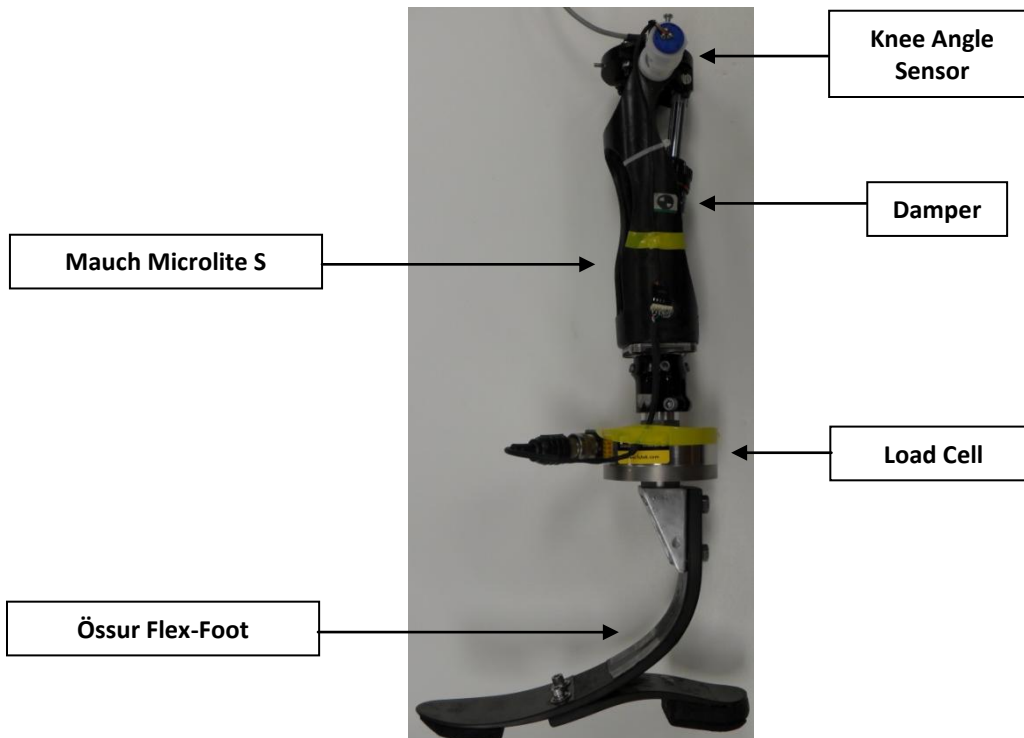


**Figure 10: Mauch Microlite S prosthesis with an Össur Flex Foot. Modifications include a load cell to read GRF and a potentiometer to measure knee angle.**

During the initial testing the center of oscillation of the vertical slide was set high enough so the Flex-Foot was not able to achieve ground contact during normal motion. This was done to verify proper operation of the system as a whole. Once proper operation was confirmed the center of oscillation of the vertical slide was lowered manually via a slider in dSpace. Lowering the center of oscillation, the prosthesis began making ground contact with the treadmill. The center of oscillation was lowered until maximum GRF readings from the load cell were the same as the maximum desired GRF from the reference gait data.

Tracking results for the both drive-stages are shown in Figures 10 and 11. Both drive-stages exhibit exceptional tracking performance. We see some degradation of the signals due to the impact forces generated during ground contact, but we accept the performance of the robot as satisfactory.

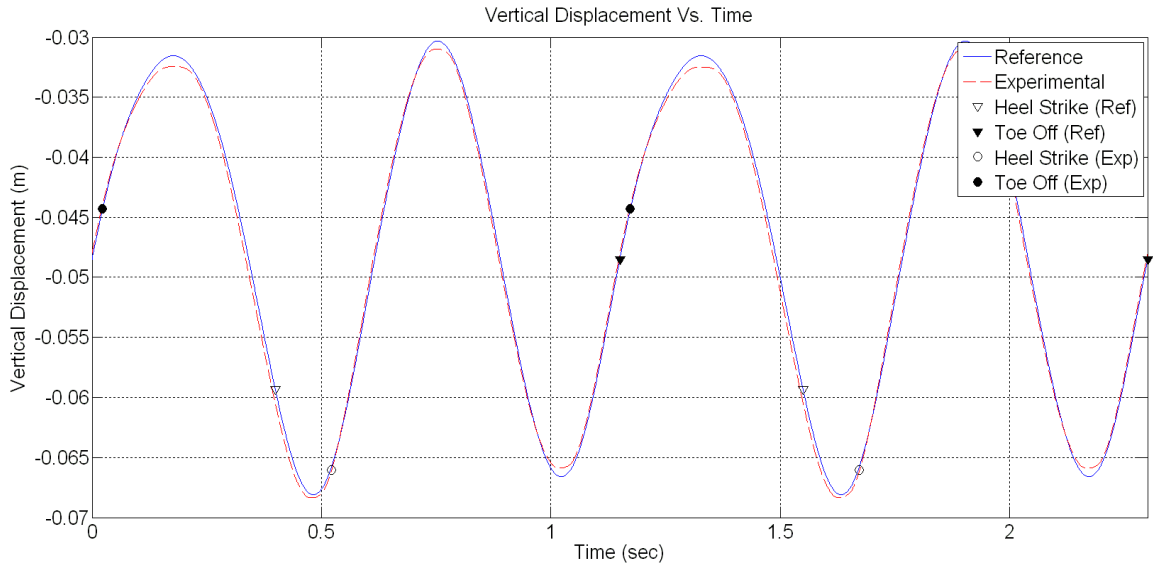


**Figure 11: Vertical displacement of robot and reference vertical displacement.**

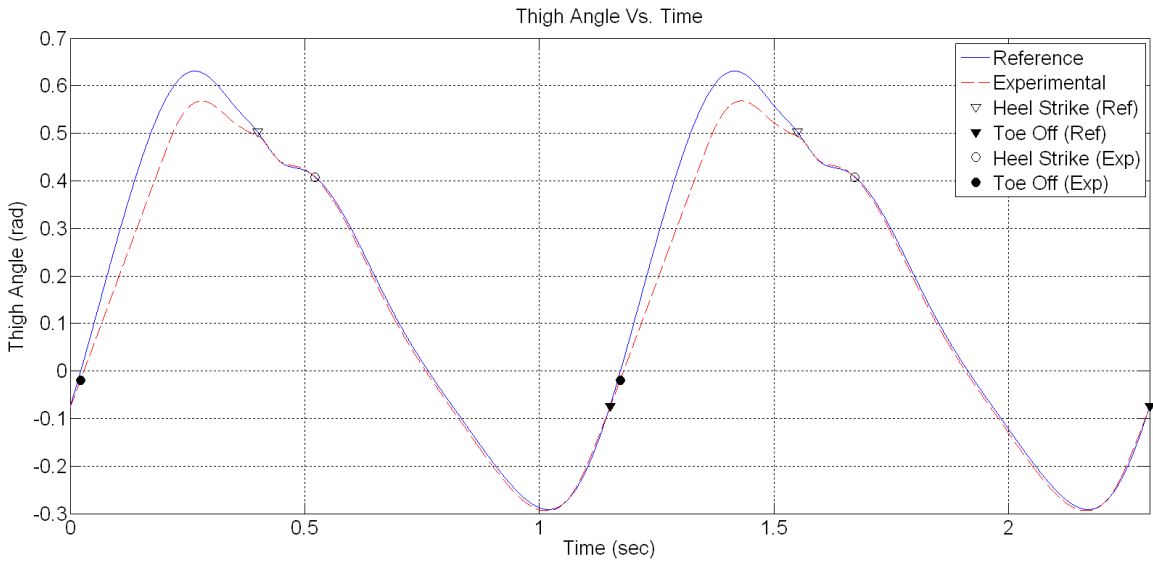


**Figure 12: Hip Angle of robot and reference hip angle.**

With tracking of the drive-stages validated, we also want to compare performance of the prosthesis with that of the reference trajectories. To do so, we examine GRF and the knee angle of the prosthesis.

Figure 12 displays knee angle of the prosthesis. We show the knee angle only for reference since it is uncontrolled. Modification of knee angle would require adjusting the manual damping settings of the prosthesis, or modifying hip movement. We measure

knee angle with a potentiometer. Performance is within range of normal human motion. However, tracking is impeded by the knee's constant damping settings and inability to produce power.

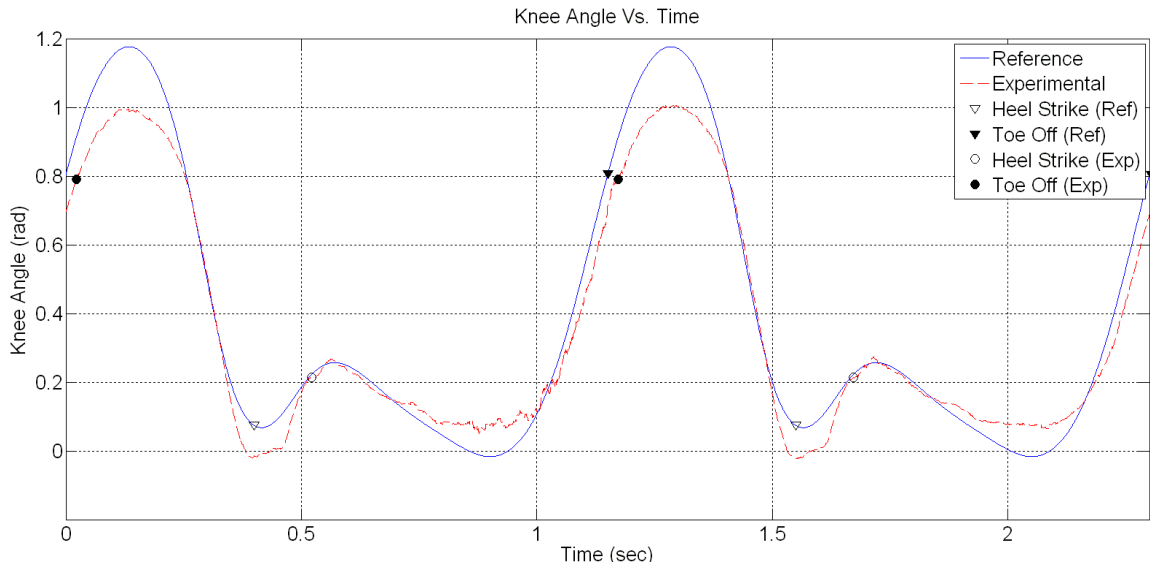


**Figure 13: Knee angle of robot and reference knee angle.**

Figure 13 is of interest because the HR has 0.74 rad of knee flexion during stance compared to 0.82 rad in the reference data, showing the Mauch Microlite to provide reasonable knee angle tracking. Typically, amputees walking with a prosthesis have little or no knee flexion during stance. This could be due to prosthesis users not trusting the knee to bear weight during stance [3]. Unlike humans the HR cannot fall during gait as it simply tracks vertical displacement and thigh angle references.

GRF of the prosthesis on the treadmill is shown in Figure 18. GRF does not follow the desired GRF closely. We attribute this to simulating able-bodied hip movement with the HR, but testing with a passive prosthesis. Stance phase length is shorter in duration than we would expect and although the double peak profile is present we see that heel strike GRF is significantly smaller with the robot.

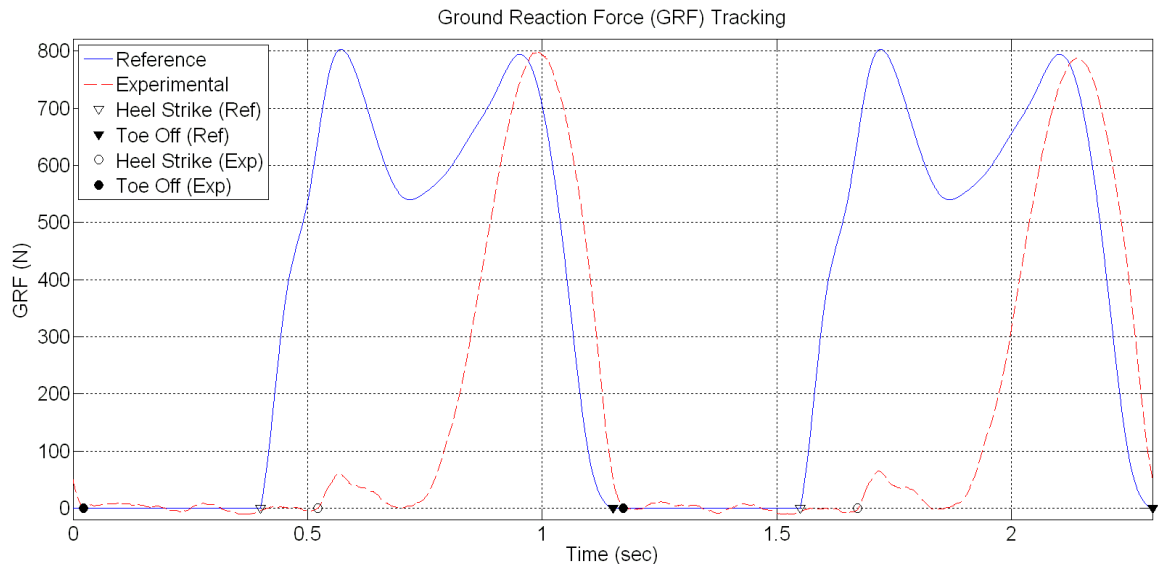


Figure 14: GRF of robot and desired GRF.

Since poor GRF tracking was observed, we want to improve this by implementing GRF control. Rather than using a typical feedback loop, a more life-like process is chosen. Since prosthesis users alter their gait in order to obtain better ambulation, we emulate this with the robot. We seek GRF control by modifying the reference hip trajectories of the HR. Therefore the HR will in effect be modifying its own reference data in order to compensate for the prosthesis.

## **CHAPTER IV**

### **GROUND REACTION FORCE CONTROL**

Throughout this Chapter we discuss the implementation of BBO to control GRF of the HR. We start in Section 4.1 with a general overview of how we apply BBO to the HR in order to control GRF. Section 4.2 provides a description BBO. In Section 4.3 we discuss the application of BBO to both the HR simulation and HR hardware. Section 4.4 presents the HR simulation. Here we explain the goals of the simulation and the simulation results. Finally in Section 5.5 we apply BBO to the HR hardware to control GRF. We apply BBO in two distinct optimization phases and discuss our final results.

#### **4.1 Overview**

The HR tracks the reference motion profiles as shown in the previous chapter. However, those results show the deficiencies of a passive prosthesis. GRF and knee angle do not follow the reference profiles. We do not address knee angle tracking since the passive prosthesis knee is uncontrollable. However, we can control GRF of the prosthesis. Rather than controlling GRF with a feedback loop, we choose to indirectly

control the GRF by adjusting the reference trajectories during the stance phase of gait. We use BBO to adjust the reference data for the HR. This will make the robot compensate for the passive prosthesis, like an actual amputee using the same prosthesis would.

## 4.2 Biogeography-Based Optimization (BBO)

BBO is an EA which uses the geographical distribution of biological species as its foundation. The study of biogeography examines the speciation, migration, mutation, and extinction of organisms in nature. BBO represents and simulates this process [6]. It has been applied to numerous problems, including aircraft engine sensor selection [6], control of wall following robots [1], electrocardiogram parameter identification [5], and prosthetic knee control [39].

In nature a habitat contains species or individuals. These individuals can migrate between habitats based on how well a habitat is suited for supporting life. We measure this as the habitat suitability index (HSI). The factors that influence HSI are suitability index variables (SIVs). An SIV can be things such as rainfall, topography, temperature, or abundance of vegetation [6]. In essence an HSI can be thought of as the dependent variable of a habitat and an SIV the independent variable [5].

A high HSI means the habitat is highly suitable for life and therefore has a high emigration rate and low immigration rate. Conversely, a habitat with low HSI has a high immigration rate and low emigration rate. An example of this is shown in Figure 19, where  $\lambda$  is the immigration rate,  $\mu$  the emigration rate, and  $S$  the number of species, which is directly correlated with HSI. Maximum immigration  $I$  to a habitat occurs when there are no species in that habitat and maximum emigration  $E$  occurs when  $S = S_{max}$ ,

the maximum number of species a habitat can support [7]. As time progresses, habitats with high HSI will dominate those with a low HSI. However, due to overcrowding in habitats, some individuals migrate to habitats with low HSI, potentially increasing the HSI of those habitats.

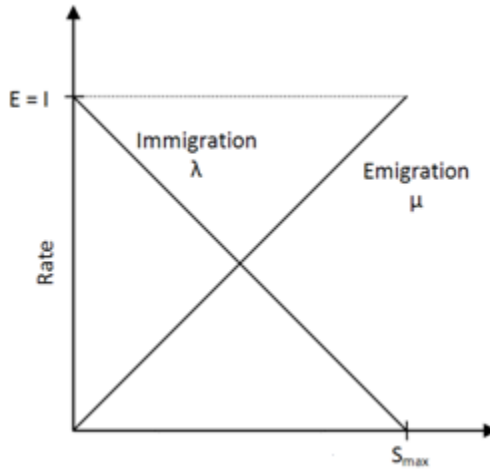


Figure 15: Immigration and emigration rates verse number of species.

In BBO we consider HSI to be a measure of how well a particular candidate solution performs, which is inversely related to the cost  $C$  of a candidate solution. SIVs are considered to be any factors that affect the HSI [1]. Individuals are represented as the independent variables we wish to optimize. We consider a habitat to be a set of individuals or candidate solutions. A population or set of candidate solutions are then tested on an optimization problem. Once the population is tested immigration and emigration rates are assigned to the candidate solutions based on cost. Migration then takes place between the individuals, or the candidate solutions, based on immigration and emigration rates. Our candidate solutions can therefore share independent variables amongst themselves. We define  $\lambda$  and  $\mu$  for the  $i$ -th candidate solution as follows:

$$\lambda_i = \frac{f_i}{n} \quad (4.1)$$

$$\mu_i = 1 - \lambda_i$$

where  $n$  represents the total number of candidate solutions in a population,  $i \in [1, n]$ ,  $n$  is the total number of candidate solutions in the BBO population, and  $f_i$  is the fitness rank of candidate solution  $i$ , where the best candidate solution has a rank of 1 and the worst has a rank of  $n$ .

Similar to many EAs, BBO also implements elitism and mutation. Elitism allows us to maintain the best candidate solution(s) from one generation to the next, assuring us that the best candidate solutions are never lost [39]. Mutation increases diversity and adds new information into the population [6].

### **4.3 Application of BBO to GRF Optimization**

We apply BBO in both simulation and hardware. In both applications BBO creates a continuous delta displacement signal which is added to the vertical displacement reference. When we apply BBO to the robot we also optimize the zero-offsets or bias of the reference data, but this is not necessary in simulation. This is discussed later in Section 4.4. Here we discuss concepts that can be applied to both the simulation and hardware applications of BBO.

We choose to add a delta displacement signal to the vertical displacement reference trajectory. This is done so the original signal is not lost, which allows us to use the original trajectory as an experimental control and initial condition. We create the delta displacement signal using a Fourier series representation. BBO optimizes the Fourier

coefficients based on error between reference GRF and experimental GRF. To ease computation we parameterize each candidate delta displacement signal as a Fourier cosine series rather than a full Fourier series:

$$u(t) = a_0 + \sum_{k=1}^M a_k \cos(2\pi kt/T) \quad (4.2)$$

where  $T$  is half of the control duration. Control duration is only during stance phase of the gait cycle.  $M$  is the number of Fourier coefficients. There are thus  $M + 1$  independent variables to be optimized in the problem.  $M$  is a tradeoff between search resolution and problem size.  $T$  is half of the signal duration so we can use the cosine series rather than the full Fourier series, which reduces the dimension of the problem by almost 50% [16].  $u(t)$  is an even function on the time interval  $t \in [-T, +T]$ , but we only apply the control signal between time 0 and  $T$ .

To change the candidate solution into a delta-displacement signal,  $u(t)$  is calculated from Equation (4.2) in real time. Since the HR uses SMC, we need an input reference signal and its first two derivatives. To calculate the first two derivatives of the delta-displacement signal, real time derivatives are calculated using a low pass filter approximation which is shown in Equation (4.3).

$$H(s) = \frac{s}{\tau s + 1} \quad (4.3)$$

where  $\tau = 1 \text{ ms}$ . Analytical derivatives could be used, however the reference data is smooth enough that the approximation works satisfactorily.

The first candidate solution tested for each BBO simulation is the Fourier coefficient set containing all zeros. This candidate solution, when added to the reference data, produces no change in the reference data. This guarantees that we will always begin

the optimization process with the original reference data as the initial condition of the BBO simulation.

#### **4.4 Hip Robot (HR) Simulation**

Before we use BBO on the HR hardware, we verify that BBO can modify the vertical displacement motion profile using a Simulink simulation developed in [20], which simulates HR operation. Doing so allows us to develop an appropriate BBO process without risking unexpected or potentially harmful behavior to the HR. The simulation utilizes a Hybrid Swing-Stance Model [20] for the HR and can predict tracking performance of both drive-stages, knee angle of the prosthesis, and GRF of the HR. The simulation utilizes the same model parameters for both drive-stages and the SMC as derived in this thesis and in [20]. We do not pursue perfect GRF tracking with the simulation due to the differences between the simulation and the robot hardware. The simulation does not have a model for a prosthetic foot. It simulates the HR's GRF by means of a single point of ground contact, or peg leg, where as the robot tests prostheses with a prosthetic foot. Therefore the simulation does not reproduce heel strike and toe off conditions appropriately, and GRF from the simulation does not adequately simulate GRF of the HR. We therefore use the simulation only to develop the BBO procedure for the HR in order to avoid potentially hazardous situations. Simulation results only confirm that the concept will be feasible on the HR hardware.

##### **4.4.1 Simulation Characteristics**

Simulations were run on a 24-core processor PC. Using MATLAB's parallel processing toolbox, simulations can run across a maximum of twelve cores. This means

that MATLAB can support 12 parallel processes or simulations. However, due to the high computational demand of the HR simulation, we were only able to use eight parallel simulations running across twelve cores. Using any more than 8 parallel simulations would cause the optimization to crash due to lack of memory.

The simulation was updated to include a series of custom-made rate-limit and saturation blocks in Simulink. These simulated the safety limits built into the robot. If any of these limits were reached, the cost for the BBO candidate solution being tested was assigned a high value as reaching these limits is undesirable.

The test sequence for the simulation is shown in Figure 16. For each candidate solution, the HR simulation was run for a series of four strides or complete gait cycles. The first two strides were used to provide the same initial conditions for each candidate solution. During these steps the simulation would be run using the unaltered reference vertical displacement. The third and fourth steps then add the delta displacement signal to the reference data. We use two steps because it was found that the HR in both simulation and in experimental hardware needed at least one step before it reached consistent operating conditions. Cost was calculated based on the GRF of the fourth gait cycle.

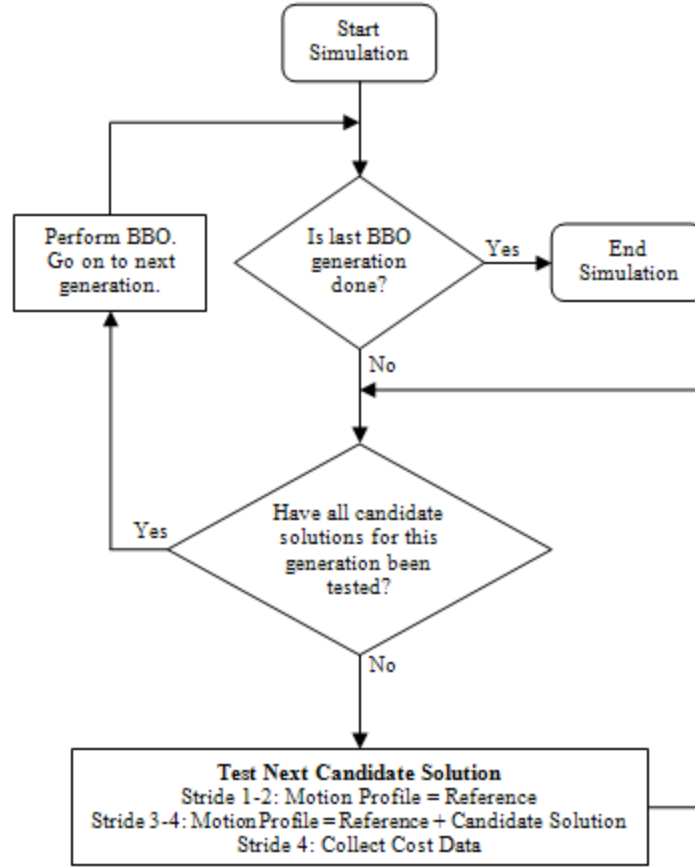


**Figure 16: Simulation Flowchart.**

Cost  $C$  for each candidate solution was only calculated during stance phase of gait since GRF is zero during swing phase. Consequently BBO is only applied during the stance phase. We calculate cost  $C$  of a solution based on the mean squared error between the reference GRF and simulated GRF:

$$C = \frac{\sum_{i=1}^N (G_{Ri} - G_{Si})^2}{N} \quad (4.4)$$

where  $N$  is the total number of time samples,  $G_{Ri}$  is the reference GRF at time step  $i$ , and  $G_{Si}$  is the simulated GRF of the robot at time step  $i$ .

#### 4.4.2 Simulation Results

BBO parameters for the simulation are shown in Table VII. We choose  $M = 7$  for a total of eight optimization coefficients. The use of eight coefficients was determined from trial and error testing with the simulation to provide a good tradeoff between resolution and problem size. Initial conditions for vertical displacement and GRF are shown in Figures 17 and 18 respectively.

<b>HR Simulation BBO Parameters</b>	
<i>Population Size</i>	40
<i>Generation Limit</i>	50
<i>Number of Elites</i>	2
<i>Number of Independent Variables</i>	8
<i>Min/Max parameter Values (rad)</i>	[-0.01 -0.01 -0.01 -0.01 -0.01 -0.01 -0.01 -0.01] [0.01 0.01 0.01 0.01 0.01 0.01 0.01 0.01]
<i>Initial Candidate Solution (rad)</i> <i>(reference profile)</i>	[0 0 0 0 0]
<i>Initial Cost</i>	$1.0203 \times 10^5$

**Table VII: HR Simulation BBO Parameters.**

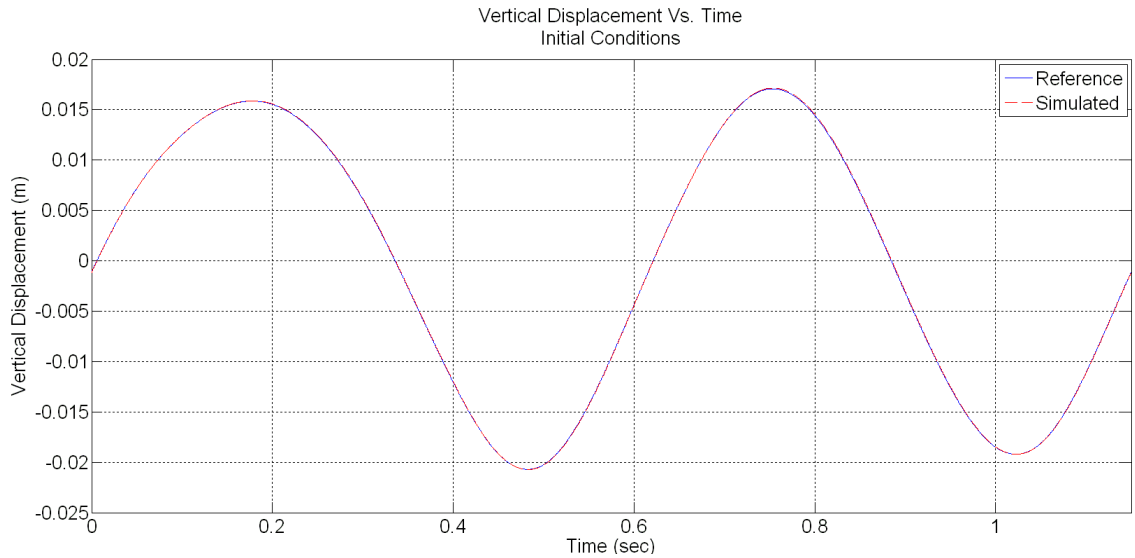


**Figure 17: Initial simulation conditions for vertical displacement of robot.**

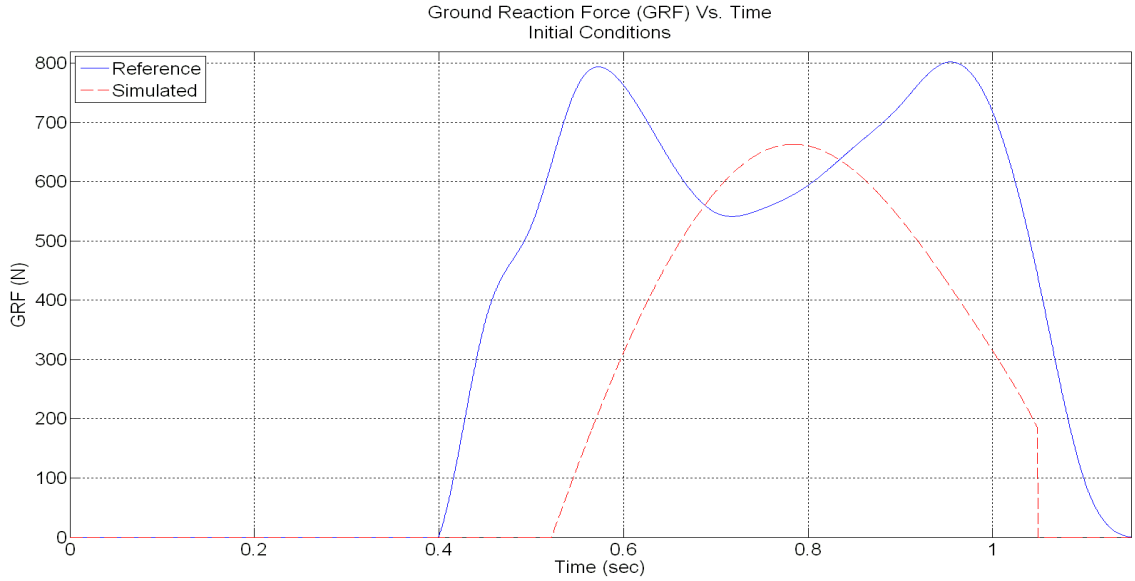


**Figure 18: Initial simulation conditions for GRF of robot. Notice that the simulated data has only one peak. This is because we are using a peg leg which cannot simulate heel strike and toe off conditions. Initial Cost =  $1.0203 \times 10^5$ .**

Running BBO lowered the cost by 32%. BBO results are shown in Table VIII with cost results, vertical displacement, and GRF shown in Figures 19, 20, and 21 respectively. Figure 19 displays the lowering of cost, confirming that we can improve GRF tracking by modifying vertical hip displacement. Figure 20 shows the modification of the vertical displacement reference. Figure 21 shows GRF tracking improvement as it now has the desired double peak shape, even though the simulation does not include a foot.

<b>HR Simulation BBO Results</b>	
<i>Best Candidate Solution (rad)</i>	[0.01258 0.012846 0.012799 0.012758 -0.011517 -0.012983 0.0090862 -0.012824]
<i>Final Cost</i>	$6.9143 \times 10^4$

**Table VIII: HR simulation BBO Results.**

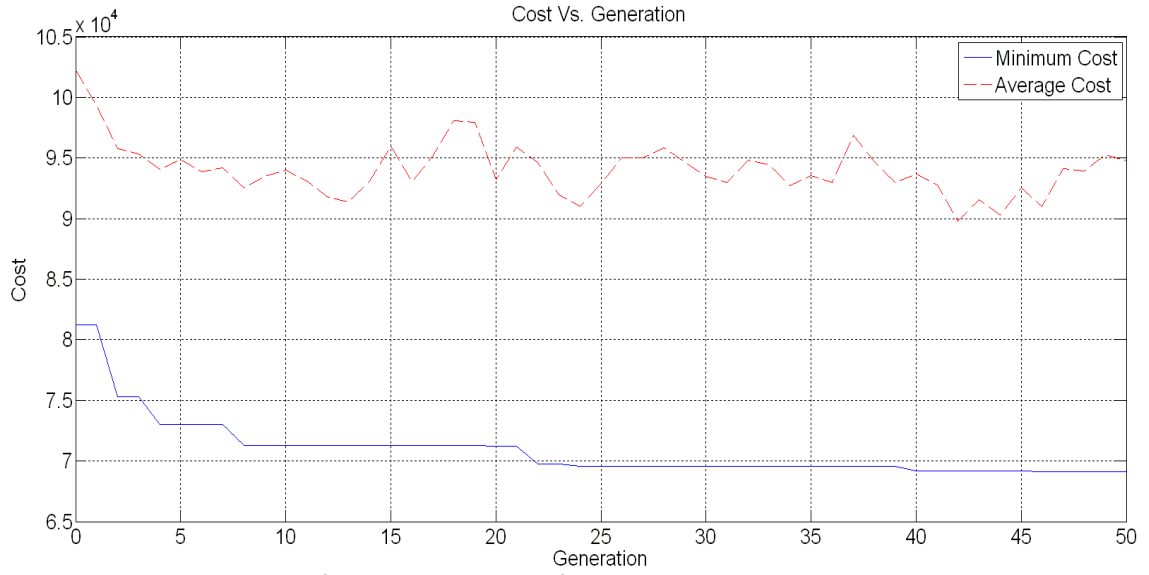


**Figure 19: Cost of candidate solutions for HR simulation over BBO generations.**

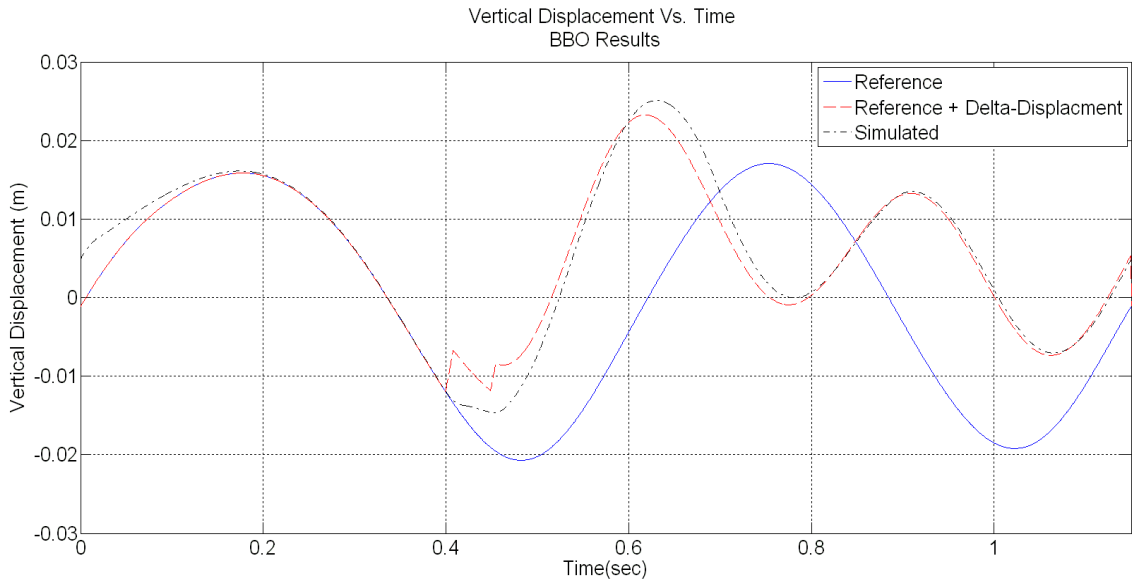


**Figure 20: Simulated vertical displacement of robot after BBO. Positive displacement represents lowering of the prosthesis.**

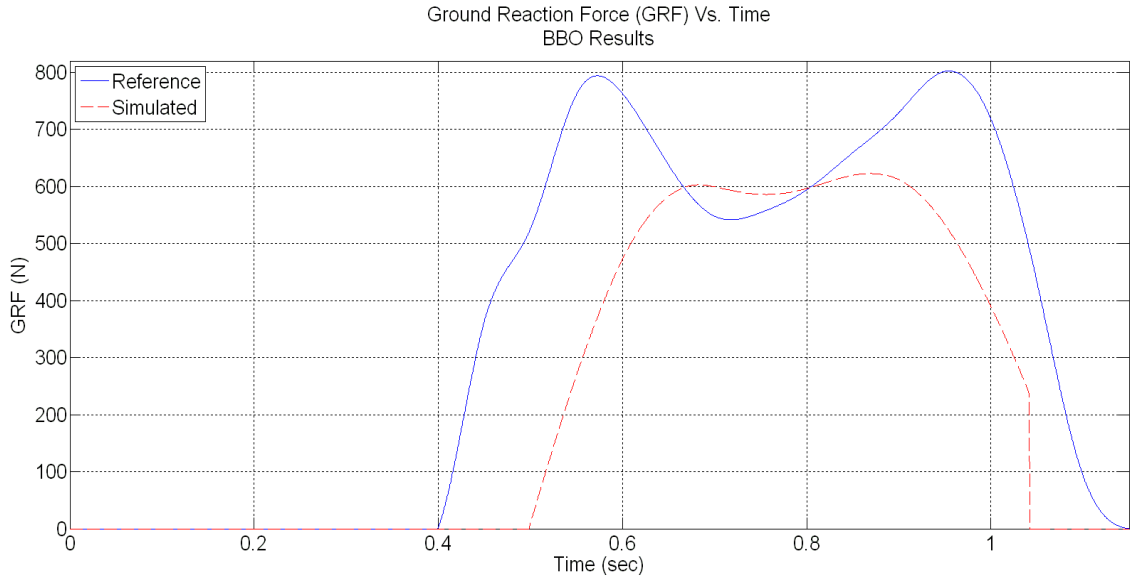


**Figure 21: Simulated GRF of robot after BBO. Final Cost =  $6.9143 \times 10^4$ .**

Notice the jagged transitions between stance and swing phase in Figure 20. This is because we optimized the  $a_0$  coefficient of the Fourier series. Therefore since the Fourier series only applies during stance phase, when we add the delta-displacement signal we are adding a zero offset to the motion profile during stance, hence the stark transition. Since we are using the simulation only as a BBO proof of concept, this is fine. When we apply BBO to the HR in the next section, we will address this by adding the zero offset over the entire motion profile, not just in stance phase, resulting in a smooth transition of the reference trajectory between swing and stance phases. This requires two BBO programs for optimization on the HR hardware, which will be discussed in detail in the following section.

#### 4.5 BBO Application to HR

We apply BBO to the robot in two different optimization phases. Phase 1 of BBO optimizes the zero-offsets, or bias, of the reference vertical displacement and thigh angle data. Phase 2 creates a continuous delta-displacement signal which is added to the

vertical displacement reference. The delta-displacement signal is created and represented using the same methods as used for the HR simulation. Phase 1 and phase 2 are discussed in more detail in Sections 4.5.1 and 4.5.2 respectively. Here we present concepts which apply to both optimization programs.

The optimization process for the robot, shown in Figure 22, differs slightly from the simulations. The robot is first brought to steady state initial operating conditions before the BBO algorithm can be started. These conditions are documented in Section 3.5. Once at initial conditions, we begin the BBO algorithm.

During the BBO run, the HR operates for six strides to test a candidate solution, versus only four strides in the simulation. This is due to the use of a load cell to collect GRF data with an inherent amount of noise. Testing the same solution twice can result in slightly different costs. Therefore, cost was averaged over three strides; hence the two additional strides. When cost for a given candidate solution was different between BBO generations, cost was averaged. This also means that minimum cost can increase from one generation to the next, even though elitism is used. However, because of the small noise level and robustness of BBO, optimization was still successful.

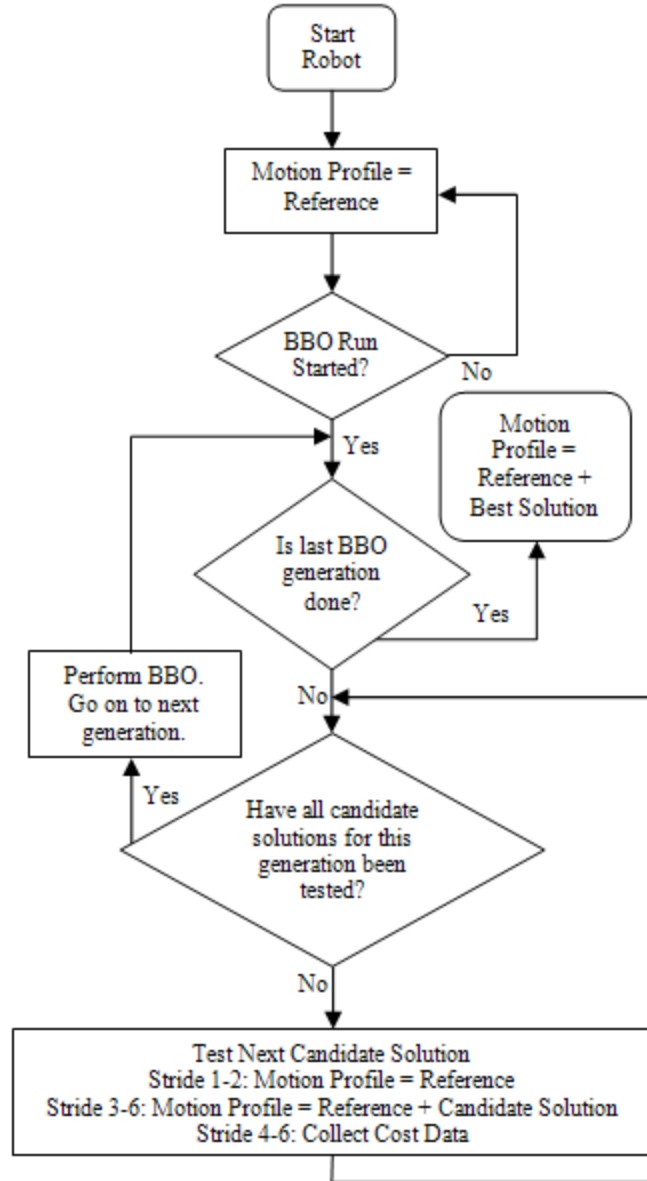


Figure 22: Flowchart of BBO process on HR.

Cost  $C$  is calculated under the same conditions as in the simulation, with one exception. The simulation had rather high costs due to the use of the mean squared error. We want smaller more manageable values for use on the HR. So we calculate cost as the root mean squared error between the reference GRF and experimental GRF  $G_{Ei}$ :

$$C = \sqrt{\frac{\sum_{i=1}^N (G_{Ri} - G_{Ei})^2}{N}} \quad (4.5)$$

#### 4.5.1 Phase 1: Bias BBO

As seen previously in simulation, varying  $\alpha_0$  in the Fourier series representation of the delta-displacement signal caused unwanted discontinuity between stance and swing phases. Rather than biasing the vertical displacement signal by means of  $\alpha_0$ , we bias the signal over the entire stride separately from the Fourier series.

During initial testing of the HR, bias of both reference trajectories was varied manually to observe its effects on GRF. GRF was very sensitive to both zero-offsets of the reference data. Varying thigh angle bias changed the heel strike and toe off conditions in the GRF profile. Adjusting the vertical displacement offset modified the magnitude of the HR's GRF. We therefore choose to optimize both zero-offsets.

Unlike BBO as applied in the simulation and later in phase 2, bias BBO in phase 1 is applied across the entire stride rather than just in stance phase. Therefore, bias is updated at the beginning of each stride rather than at the start of stance phase.

Optimization could not be completed using one BBO run because of the small safe operating ranges of the robot. Generally, both thigh-angle bias and vertical-displacement bias are lowered to achieve a better GRF. However if one of these values was lowered too far, the HR would enter an unsafe operating condition. To remain in safe operation both values must be lowered together. To accomplish this, a set of two BBO runs were completed. We refer to these as phases 1.1 and 1.2.

To determine the initial safe search space, the HR was first brought to normal operating conditions (zero biases). Thigh angle bias and vertical displacement bias were

then adjusted manually until the limits of the HR were approached. Search space parameters were determined using the same method for phase 1.2. However, the robot was initially brought to the biases determined in phase 1.1 instead of normal operating conditions.

Initial conditions and parameters for both bias BBO phases are shown in Table IX. Note that the initial candidate solution  $[0, 0]$  for phase 1.2 is not contained within the min/max parameter values. The initial population in phase 1.2 is random and therefore possible to contain poor candidate solutions. We test the initial condition from phase 1.1 to verify the improvement in phase 1.2.

<b>Bias BBO Parameters</b>		
<b><i>Both Phases</i></b>	<i>Population Size</i>	10
	<i>Generation Limit</i>	12
	<i>Number of Elites</i>	2
	<i>Number of Independent Variables</i>	2
	<i>Initial Candidate Solution (rad)</i>	[0 0]
	<i>Initial Cost</i>	390.75
<b><i>Phase 1.1</i></b>	<i>Min/Max parameter Values (rad)</i>	[-0.1300 0.0000]
	<i>Best Candidate Solution (rad)</i>	[0.0000 2.400]
	<i>Best Cost</i>	[-0.1299 2.3757]
	<i>Best Cost</i>	251.54
<b><i>Phase 1.2</i></b>	<i>Min/Max parameter Values (rad)</i>	[-0.1300 2.0265]
	<i>Best Candidate Solution (rad)</i>	[0.1183 5.5000]
	<i>Best Cost</i>	[-0.1253 4.8170]
	<i>Best Cost</i>	197.61

**Table IX: Bias BBO (Phase 1) parameters as applied to the HR.**

Results for the bias optimization runs are also shown in Table IX. Phases 1.1 and 1.2 took approximately 14 minutes each to run on the hardware. Convergence results are shown in Figure 23. Cost was lowered to  $C = 251.54$  in phase 1.1 and lowered further to  $C = 197.61$  in phase 1.2. Overall reduction in cost is 49% from the initial condition.

Robot operation with the biased signals and resultant GRFs are shown in Figures 24, 25,

and 26. Results from both bias phases are shown in the figures to display progression through phase 1. Final bias BBO results show vertical displacement was lowered by 9.73 mm and thigh angle biased by  $-0.1253$  rad from the reference trajectories. GRF tracking in phase 1.2 is much better except during the middle of stance phase when both heel and toe are in contact with the ground.

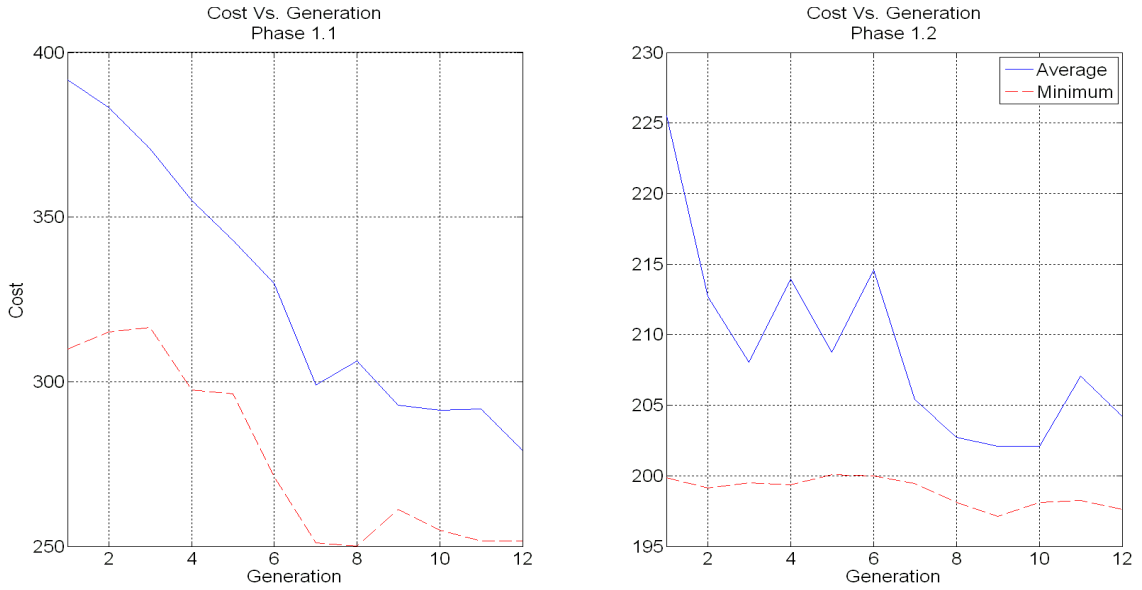


**Figure 23: Cost of BBO candidate solutions for bias optimization.**

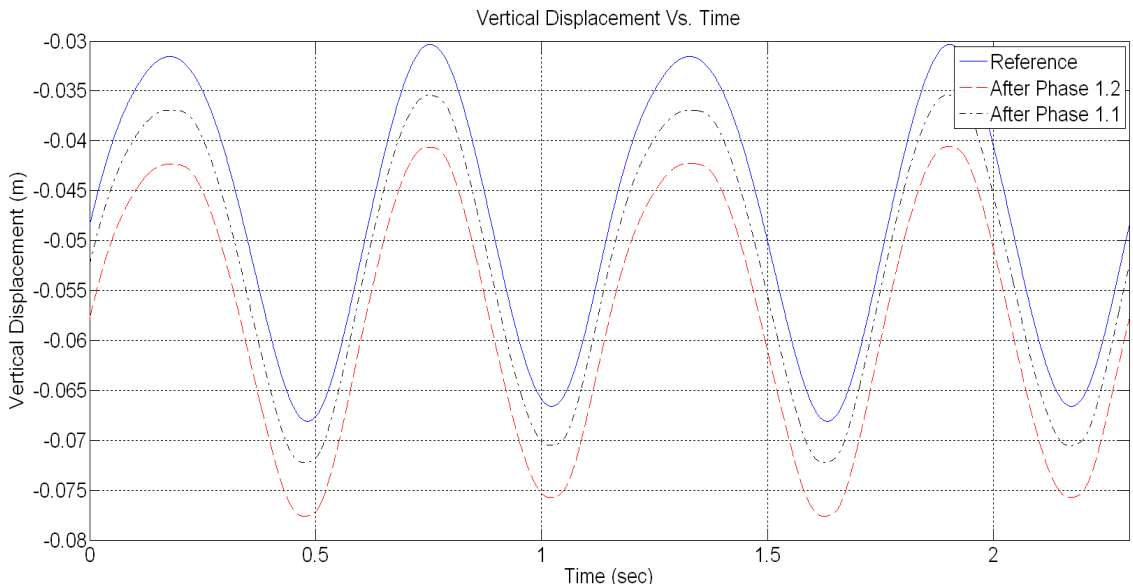


**Figure 24: Vertical displacement after bias BBO. Notice the lowering of the vertical displacement compared to the reference in both phases of optimization.**

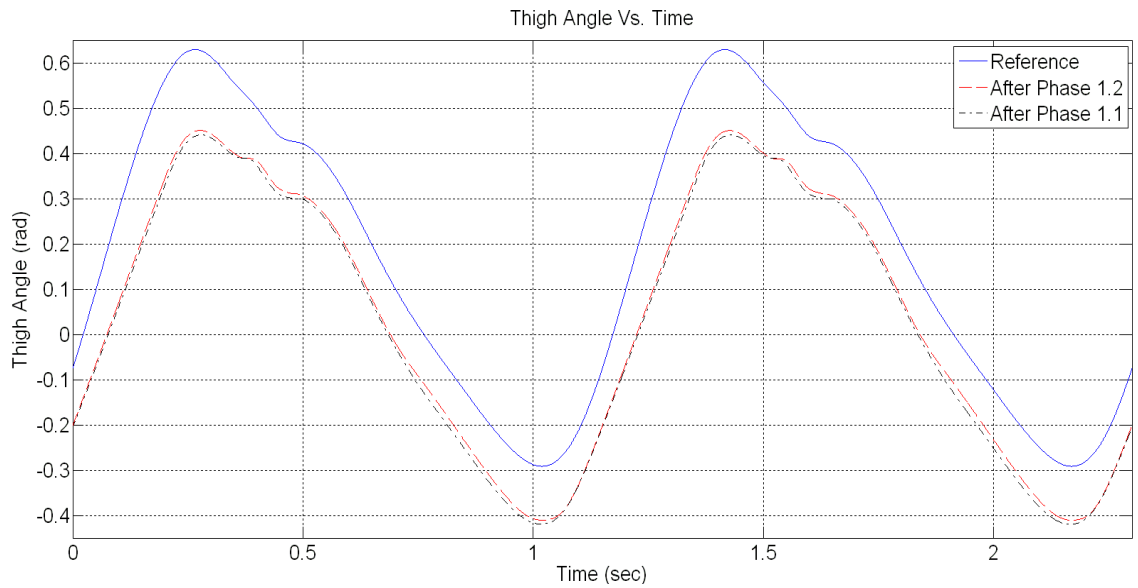


**Figure 25: Thigh angle after bias BBO run. Notice the lowering of the thigh angle in phase 1.1 and a slight increase in bias after phase 1.2.**

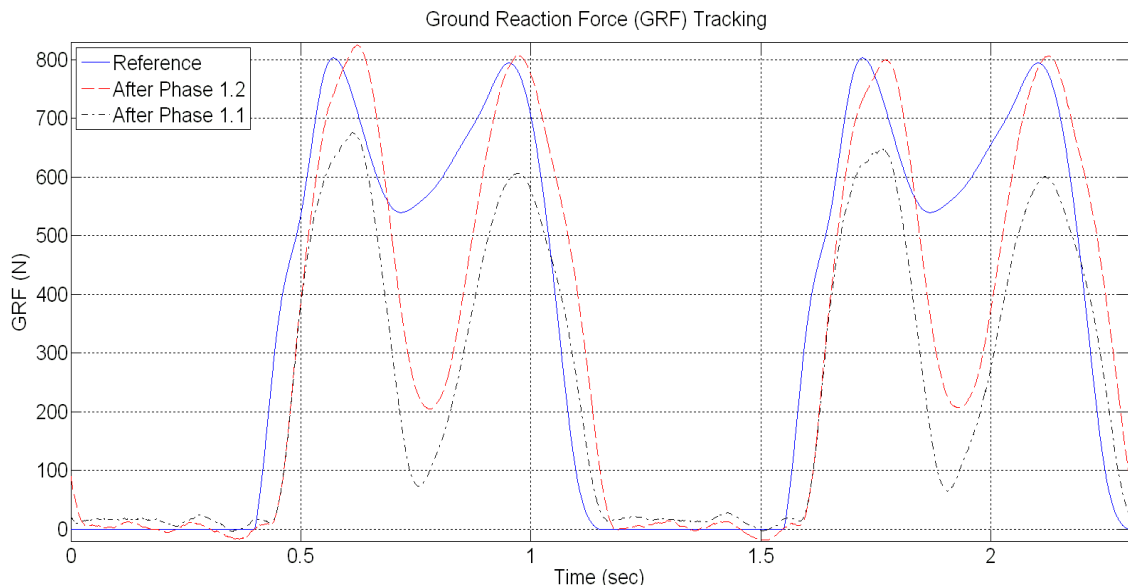


**Figure 26: GRF of robot after bias BBO. Notice the low GRF during the middle of stance phase. Also note the difference in GRF between strides due to sensor noise. The increase in GRF between optimization phases is due to the decreased vertical displacement bias. After phase 1.2, GRF Cost = 197.61.**

#### 4.5.2 Phase 2: Delta-Displacement BBO

With the zero offsets optimized in phase 1, GRF of the HR fits well with the heel strike peak and toe off peak of the reference GRF. Since thigh angle bias has the predominant effect on heel strike and toe off conditions, we do not change thigh angle

any further. Therefore, in phase 2 we only modify the vertical displacement signal in an attempt to increase GRF during the middle of stance phase when both heel and toe of the foot are in contact with the ground.

The vertical displacement signal is modified using the same methods as in the simulation. We add a delta-displacement signal to the reference data during stance phase. We use a Fourier cosine representation as shown in Equation (4.2) to represent the delta-displacement signal. We decrease the problem size to  $M = 6$  for a total of seven independent variables. This proved to be a better tradeoff between problem size and search resolution when applied to the HR hardware. To ensure a smooth transition when adding the delta-displacement signal to the reference data, and because bias offset has already been optimized, we constrain the Fourier coefficient  $a_0 = 0$ .

Parameters for optimization phase 2 are shown in Table X. Note that we apply the results from phase 1.2 as initial conditions. The initial candidate solution tested is the Fourier coefficient set  $[0 \ 0 \ 0 \ 0 \ 0 \ 0 \ 0]$ , or the unaltered biased reference data. This guarantees that we will begin optimizing from the results of phase 1, and that we can only improve from that point.

<b>Delta-Displacement BBO Parameters</b>	
<i>Population Size</i>	25
<i>Generation</i>	30
<i>Number of Elites</i>	2
<i>Number of Independent Variables</i>	7
<i>Min/Max parameter Values (rad)</i>	$[0 \ -0.72 \ -0.72 \ -0.72 \ -0.72 \ -0.72 \ -0.72]$ $[0 \ 0.72 \ 0.72 \ 0.72 \ 0.72 \ 0.72 \ 0.72]$
<i>Initial Candidate Solution (rad)</i>	$[0 \ 0 \ 0 \ 0 \ 0 \ 0 \ 0]$
<i>Reference Biases (rad)</i>	$[-0.1253 \ 4.8170]$
<i>Initial Cost (Biased Reference)</i>	197.61
<i>Best Candidate Solution (rad)</i>	$[0 \ 0.702 \ 0.108 \ -0.688 \ 0.329 \ 0.235 \ 0.609]$
<i>Best Cost</i>	148.33

**Table X: Delta-displacement BBO parameters as applied to the HR.**

Results of the BBO run are shown in Table X, with performance shown in Figure 27. Phase 2 took approximately 1 hour and 20 minutes to run on the robot hardware. BBO lowered the cost to  $C = 149.33$ , or by 62% from the reference data. Figure 28 shows the modified vertical displacement signal compared to the original reference data and the biased initial conditions. We show the biased vertical displacement to demonstrate the effect of the delta-displacement signal. Thigh angle is the same as phase 1.2 as shown in Figure 25. The improved GRF profile is shown in Figure 29, effectively showing the robot compensating for the prosthesis.

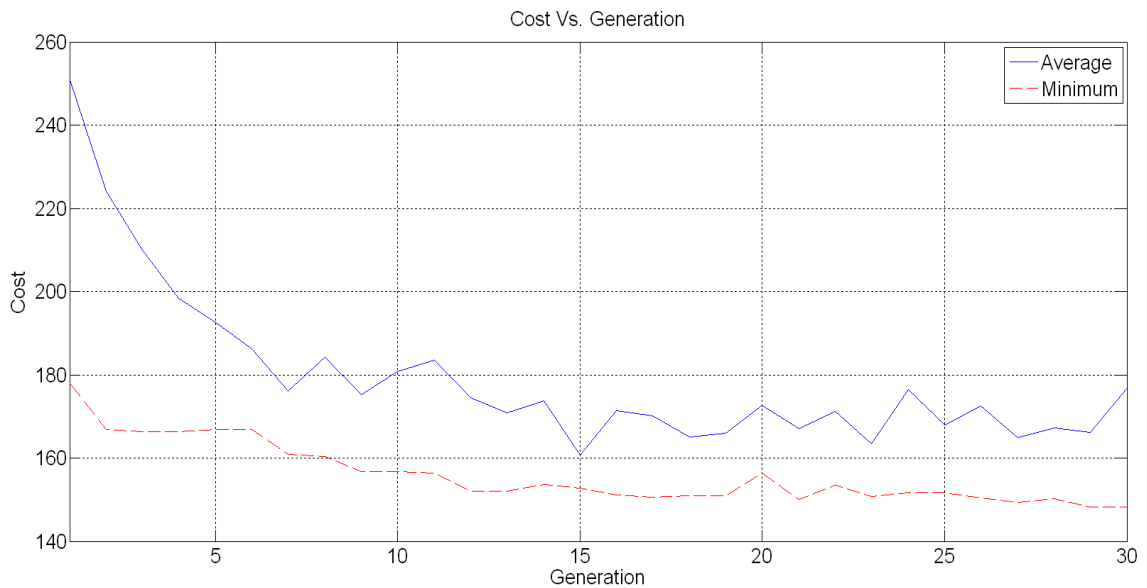


**Figure 27: Cost of BBO candidate solutions for delta-displacement optimization.**

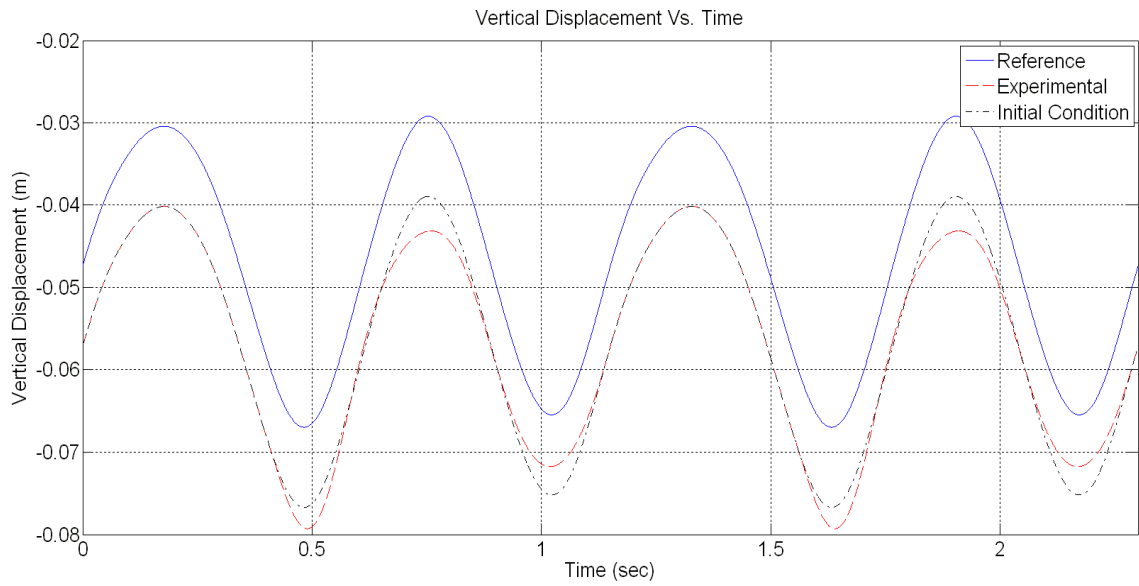


**Figure 28: Vertical displacement after delta-displacement BBO. Initial condition is the final condition of bias BBO. This plot shows the effect of the delta-displacement signal.**

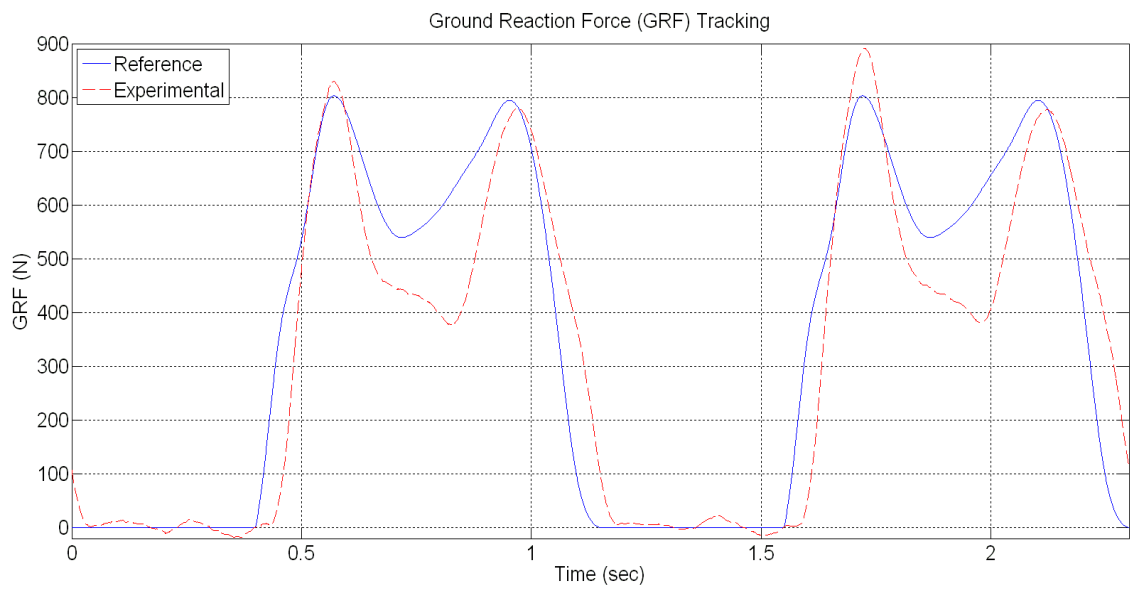


**Figure 29: GRF of the robot after delta-displacement BBO. Notice the increased GRF during middle of stance phase compared to Figure 27. GRF Cost = 148.33.**

## **CHAPTER V**

### **CONCLUSION**

#### **5.1 Summary**

We have discussed and summarized problems associated with the testing of prostheses on human subjects. We propose the use of a HR to facilitate prosthesis testing. The HR emulates the movements of a human hip and allows prostheses to be tested under conditions not possible with human subjects.

We use feedback control on the HR to track the human hip motions used as references. Thigh angle and vertical displacement are tracked. We develop SMCs for both drive stages in order to track reference inputs. Results show exceptional tracking of both drive stages.

The hip motions used as references are shown to have limitations due to discontinuities in the derivatives. Because SMC requires smoothness of the reference signal and its first two derivatives, we adjust the reference data accordingly. We apply a spline-based smoothing algorithm to optimize the data so that SMC can be used without any problems with derivative discontinuities.

We apply BBO to control the GRF of the robot. We modify the reference hip motions using BBO to simulate a prosthesis user compensating for a prosthesis. A simulation of the HR is used to design test procedures for the HR. Using the simulation, we also confirm the feasibility of modifying vertical hip displacement of the HR in order to improve GRF tracking.

Applying BBO to the HR required two distinct optimization programs. We first optimized bias for both thigh angle and vertical displacement reference data. Next a delta-displacement signal was added to the reference vertical displacement data to modify the reference data further. The delta-displacement signal was optimized using BBO. Results show a 62% improvement in GRF tracking of the HR as compared to that obtained with the original reference gait data.

## **5.2 Future Work**

To improve the results shown here and make these tests more applicable to other prostheses, a few things need to be adapted. Generally, when BBO is used, it would be applied for many generations – for example, up to 100,000 generations in [5]. While that would be unfeasible with the robot, a modest increase from this thesis would be an improvement. Due to the time demands of these tests, including taking six strides per candidate solution, the robot was only run for a maximum of 30 generations at a time. Lowering the number of strides to test a solution would allow an increase in the number of generations. We could lower the number of necessary strides by designing a new GRF measurement system, or perhaps by purchasing a load cell with less noise.

In the results, GRF of the robot/prosthesis combination always had a small time delay compared to the desired signal. Adding the delta-displacement signal to the

reference trajectory was always done during the stance phase as defined by the reference data. Since we are modifying the reference data in order to improve GRF, we could allow a slight time shift when adding the delta-displacement signal when it is added to the reference data.

When applying BBO, the real-time derivative of the delta displacement signal added to the reference data was calculated using a low pass filter approximation for input to SMC. This was done for ease of coding. We could avoid this approximation by calculating the derivatives of the Fourier series representing the delta-displacement signal. The derivatives of the delta-displacement signal could then be added to the corresponding derivatives of the reference data, avoiding the need for a real time approximation.

Finally, we would like to adapt these tests and apply them to other prostheses.

## REFERENCES

- [1] A. Shah, *Distributed Biogeography Based Optimization for Mobile Robots*, Master's Thesis, Cleveland State University, Cleveland, OH, 2009.
- [2] A. van den Bogert, S. Samorezov, B. Davis, and W. Smith, "Modeling and Optimal Control of an Energy-Storing Prosthetic Knee," *Journal of Biomechanical Engineering*, vol. 134, no. 5, pp. 0510071-0510078, 2012.
- [3] A. Segal, M. Orenduff, G. Klute, M. McDowell, J. Pecoraro, J. Shofer, and J. Czerniecki, "Kinematic and Kinetic Comparisons of Transfemoral Amputee Gait Using C-Leg and Mauch SNS® Prosthetic Knees," *Journal of Rehabilitation Research and Development*, vol. 43, no. 7, pp. 857-870, 2006.
- [4] C. Lin, P. Chang, and J. Luh, "Formulation and Optimization of Cubic Polynomial Joint Trajectories for Industrial Robots," *IEEE Transactions on Automatic Control*, vol. AC-28, no. 12, pp. 1066-1073, 1983.
- [5] D. Sadey, *Parameter Identification for the generation of Dynamic Electrocardiograms*, Honor's Thesis, Cleveland State University, Cleveland, OH, 2012.
- [6] D. Simon, "Biogeography-Based Optimization," *IEEE Transactions on Evolutionary Computation*, vol. 12, no. 6, pp. 702-713, 2008.
- [7] D. Simon, *Evolutionary Optimization Algorithms*, John Wiley & Sons, 2013.
- [8] D. Simon and C. Isik, "The Generation and Optimization of Trigonometric Joint Trajectories for Robotic Manipulators," *Proceedings of the American Control Conference*, Boston, MA, pp. 2027-2032, 1991.

- [9] D. Simon and C. Isik, "Optimal Trigonometric Robot Joint Trajectories," *Robotica*, vol. 9, pp. 379-386, 1991.
- [10] D. Simon, "Optimal Robot Motions for Repetitive Tasks," *Proceedings of the 31<sup>st</sup> Conference on Decision and Control*, Tucson, AZ, pp. 3130-3134, 1992
- [11] D. Winter, *Biomechanics and Motor Control of Human Gait*, 2<sup>nd</sup> Edition, University of Waterloo Press, 1991.
- [12] F. Sup, A. Bohara, and M. Goldfarb, "Design and Control of a Powered Knee and Ankle Prosthesis: Initial Evaluation on a Transfemoral Amputee," *IEEE International Conference on Robotics and Automation*, Rome, Italy, pp. 4134-4139, 2007.
- [13] F. Sup, A. Bohara, and M. Goldfarb, "Design and Control of a Powered Transfemoral Prosthesis," *The International Journal of Robotics Research*, vol. 27, no. 2, pp. 263-273, 2008.
- [14] F. Sup, H. Atakan, J. Mitchell, T. Withrow, and M. Goldfarb, "Design and Control of an Active Electrical Knee and Ankle Prosthesis," *IEEE RAS EMBS International Conference on Biomedical Robotics and Biomechatronics*, Scottsdale, AZ, pp. 523-528, 2008.
- [15] F. Sup, H. Atakan, J. Mitchell, T. Withrow, and M. Goldfarb, "Self-Contained Powered Knee and Ankle Prosthesis: Initial Evaluation on a Transfemoral Amputee," *IEEE International Conference on Rehabilitation Robotics*, Kyoto, Japan, pp. 638-644, 2009.

- [16] G. Konidaris, S. Osentoski, and P. Thomas. “Value function approximation in reinforcement learning using the Fourier basis,” *Twenty-Fifth Conference on Artificial Intelligence*, San Francisco, California, pp. 1468-1473, 2011.
- [17] G. Nandi, A. Ijspeert, P. Chakraborty, and A. Nandi, “Development of Adaptive Modular Active Leg (AMAL) Using Bipedal Robotics Technology,” *Robotics and Autonomous Systems*, vol. 57, no. 6, pp. 603-616, 2009.
- [18] G. Thomas, T. Wilmot, S. Szatmary, D. Simon, and W. Smith, “Evolutionary Optimization of Artificial Neural Networks for Prosthetic Knee Control,” *Efficiency and Scalability Methods for Computational Intellect*, (B. Igel'nik and J. Zurada, editors), Chap. 7, pp. 142-161, IGI Global, 2013.
- [19] H. Richter, *Advanced Control of Turbofan Engines*, Springer Science + Business Media, 2012.
- [20] H. Richter and D. Simon, “Robust Tracking Control of a Prosthesis Test Robot”, *to appear in ASME Journal of Dynamic Systems*, 2014.
- [21] I. Pappas, M. Popovic, T. Keller, V. Dietz, and M. Morari, “A Reliable Gait Phase Detection System,” *IEEE Transactions on Neural Systems and Rehabilitation Engineering*, vol. 9, no. 2, pp. 113-125, 2001.
- [22] J. Johansson, D. Sherrill, P. Riley, P. Bonato, and H. Herr, “A Clinical Comparison of Variable-Damping and Mechanically Passive Prosthetic Knee Devices,” *American Journal of Physical Medicine & Rehabilitation*, vol. 84, no. 8, pp. 563-575, 2005.
- [23] K. Zemalache, M. Tahar, A. Omari, and H. Maaref, “Sliding Mode Control Technique: Application to a Four Rotors Mini-Flying Robot,” *Intelligent*

- Systems and Automation, 2<sup>nd</sup> Mediterranean Conference*, vol. 1107, no. 1, pp. 160-165, 2009.
- [24] L. Graham, D. Datta, B. Heller, and J. Howitt, "A Comparative Study of Conventional and Energy-Storing Prosthetic Feet in High-Functioning Transfemoral Amputees," *Archives of Physical Medicine & Rehabilitation*, vol. 88, no. 7, pp. 801-806, 2007.
- [25] M. Bellman, T. Schmalz, and S. Blumentritt, "Comparative Biomechanical Analysis of Current Microprocessor-Controlled Prosthetic Knee Joints," *Archives of Physical Medicine & Rehabilitation*, vol. 91, no. 4, pp. 644-652, 2010.
- [26] N. Ghani, N. Yatim, and N. Azmi, "Trajectory Tracking of Two Wheels Mobile Robot Using Sliding Mode Control," *Proceedings of the Fourth Global Conference on Power Control and Optimization*, vol. 1337, no. 1, pp. 135-139, 2011.
- [27] P. A. Lilley, M. Raine, and G.W. Blunn, "In Vitro Generation of Replacement Knee Wear by Simulation," *Proceedings of International Conference on Simulation*, York, UK, pp. 35-41, 1998.
- [28] P. A. Lilley, M. Raine, and G.W. Blunn, "Simulation of the Wear of Metal Implants by Soft-Tissue," *Proceedings of International Conference on Simulation*, York, UK, pp. 42-49, 1998.
- [29] R. Davis, H. Richter, D. Simon, and A. van den Bogert, "Evolutionary Optimization of Ground Reaction Force for a Prosthetic Leg Testing Robot," *Submitted to the American Control Conference 2014 for publication*.

- [30] R. Gailey, K. Allen, J. Castles, J. Kucharik, and M. Roeder, "Review of Secondary Physical Conditions Associated with Lower-Limb Amputation and Long-Term Prosthesis Use," *Journal of Rehabilitation & Development*, vol. 45, no. 1, pp. 15-20, 2008.
- [31] R. Robinson, C. Kothera, B. Woods, R. Vocke, and N. Wereley, "High Specific Power Actuators for Robotic Manipulators," *Journal of Intelligent Material Systems and Structures*, vol. 22, no. 13, pp. 1501-1511, 2011.
- [32] R. Williams, A. Turner, M. Orenduff, A. Segal, G. Klute, J. Pecoraro, and J. Czerniecki, "Does Having a Computerized Prosthetic Knee Influence Cognitive Performance During Amputee Walking?" *Archives of Physical Medicine & Rehabilitation*, vol. 87, no. 7, pp. 989-994, 2006.
- [33] S. Au, P. Bonato, and H. Herr, "An EMG-Position Controlled System for an Active Ankle-Foot Prosthesis: An Initial Experimental Study," *Proceedings of the 2005 IEEE International Conference on Rehabilitation Robotics*, Chicago, IL, pp. 375-379, 2005.
- [34] S. Chand and K. Doty, "On-Line Polynomial Trajectories for Robot Manipulators," *The International Journal of Robotics Research*, vol. 4, no. 2, pp. 38-48, 1985.
- [35] S. Thompson and R. Patel, "Formulation of Joint Trajectories for Industrial Robots Using B-Splines," *IEEE Transactions on Industrial Electronics*, vol. IE-34, no. 2, pp. 192-199, 1987.
- [36] T. Bae, K. Choi, D. Hong, and M. Mun, "Dynamic Analysis of Above-Knee Amputee Gait," *Clinical Biomechanics*, vol. 22, no. 5, pp. 557-566, 2006.

- [37] T. Chin, K. Machida, S. Sawamura, R. Shiba, H. Oyabu, Y. Nagakura, I. Takase, and A. Nakagawa, "Comparison of Different Microprocessor Controlled Knee Joints on the Energy Consumption During Walking in Trans-Femoral Amputees: Intelligent Knee Prosthesis (IP) versus C-Leg," *Prosthetics and Orthotics International*, vol. 30, no. 1, pp. 73-80, 2006.
- [38] T. Wilmot, G. Thomas, B. Montavon, R. Rarick, A. van den Bogert, S. Szatmary, D. Simon, W. Smith, and S. Samorezov, "Biogeography-Based Optimization for Hydraulic Prosthetic Knee Control," *Medical Cyber-Physical Systems Workshop*, Philadelphia, PA, pp. 18-25, 2013.
- [39] T. Wilmot, *Intelligent Controls for a Semi-Active Hydraulic Prosthetic Knee*, Master's Thesis, Cleveland State University, Cleveland, OH, 2011.
- [40] W. Dyck, S. Onyshko, D. Hobson, D. Winter, and A. Quanbury, "A Voluntarily Controlled Electrohydraulic Above-Knee Prosthesis," *Bulletin of Prosthetics Research*, vol. 10, no. 23, pp. 169-186, 1975.
- [41] X. Yu and O. Kaynak, "Sliding-Mode Control with Soft Computing: A Survey," *IEEE Transactions on Industrial Electronics*, vol. 56, no. 9, pp. 3275-3285, 2009.
- [42] 2013, *Flex-Foot Feet* [Online], Available:  
<http://www.ossur.com/?PageID=12639>
- [43] 2013, *Mauch Knee* [Online], Available:  
<http://www.ossur.com/?PageID=12644>

## **APPENDICES**

## APPENDIX A: Wiring Lists and Schematics

Here the overall wiring lists and schematics are shown for the HR. In order for proper operation, all wires shown in the following schematics must be connected. The wiring is broken up into subsections for ease of problem diagnosis. Each list provides connection information for both ends of a wire as well as color information for any internal conductor(s) within that wire. An example list is shown below detailing the content found within each list.

### Example Schematic Name

Cable Name			
End 1	Main Shielding Color	Conductor(s)	End 2
Connection Location: Terminal (if needed)	Main color of shielding for multiple conductor wires or color of single conductor	Color of internal conductors for multiple conductors or shielding color for single wires.	Connection Location: Terminal (if needed)

### Acronyms Found in Wiring Lists:

**NC** Not Connected

**LM** Linear Motor

**TB** Terminal Board

**RM** Rotary Motor

**BM** Braking Module

**CB** Control Box

**Emg** Emergency

**MC** Microcontroller

**QD** Quick Disconnect

**LC** Load Cell

## Linear Motor: Main Power and Encoder

<b>3 Phase Power</b>			
3 Phase Power Outlet	Black	Black	Twist Connected with: Black from L1 L2 Power and Black from L11 L21 Power
		Tan	Twist Connected with: Blue from L1 L2 Power and Blue from L11 L21 Power
		Brown	NC

<b>L1 L2 Power</b>			
Twist Connected with Black from 3 Phase Power and Black from L11 L21 Power	Black	Black	LM Servo: L1
Twist Connected with Tan from 3 Phase Power and Blue from L11 L21 Power		Blue	LM Servo: L2
NC		Green	NC

<b>L11 L21 Power</b>			
Twist Connected with Black from 3 Phase Power and Black from L1 L2 Power	Black	Black	LM Servo: L11
Twist Connected with Tan from 3 Phase Power and Blue from L1 L2 Power		Blue	LM Servo: L21
NC		Green	NC

<b>P1 P2 Jumper</b>			
LM Servo: P1	Black	Black	LM Servo: P2

<b>P D Jumper</b>			
LM Servo: P	Black	Black	LM Servo: D

<b>LM Power</b>			
LM Servo: U	Black	Red	Linear Motor
LM Servo: V		White	
LM Servo: W		Black	
LM Servo: PE		Green	

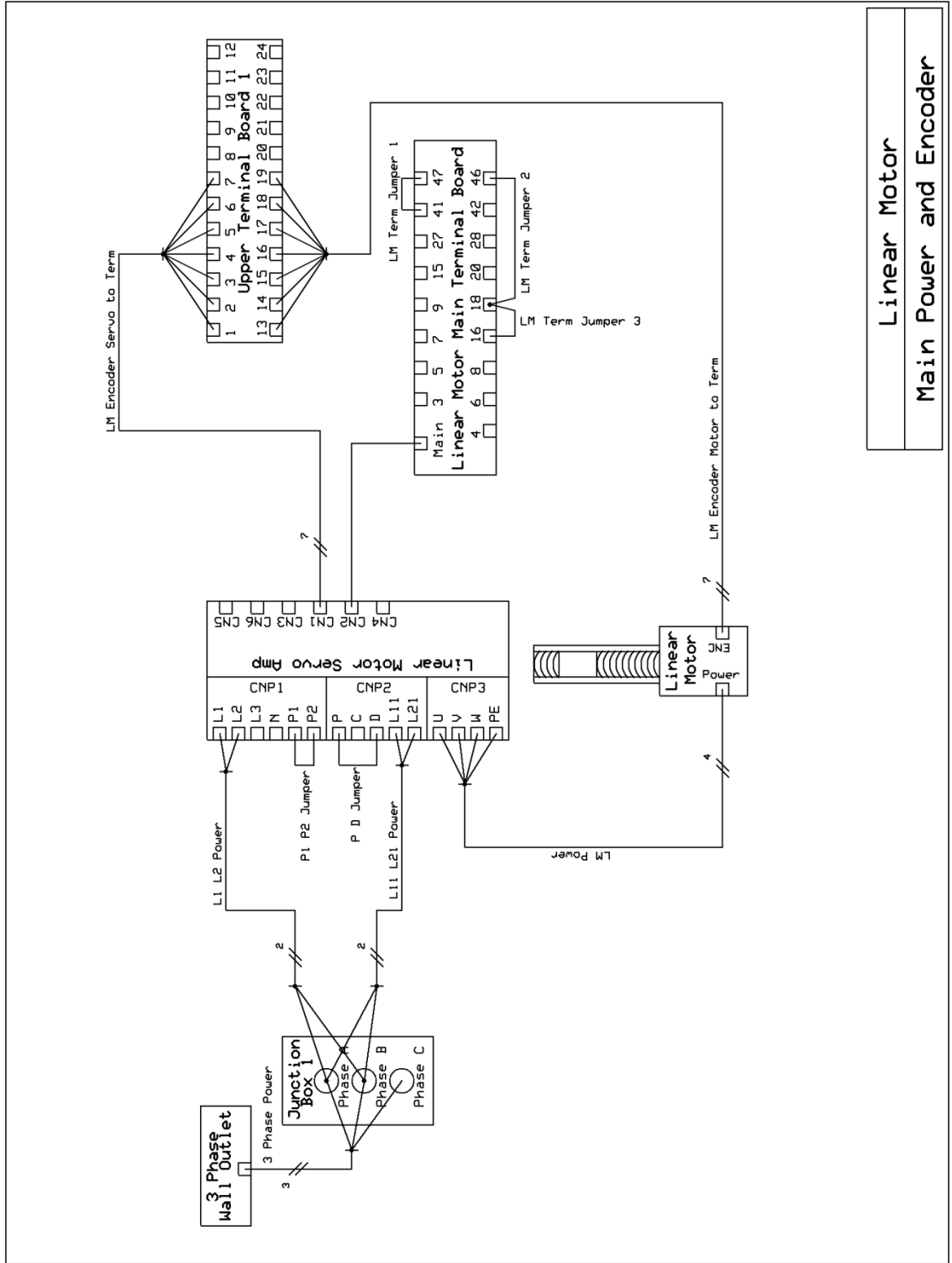
<b>LM Encoder Servo to Term</b>			
LM Servo: CN1	Black	Grey	Upper TB 1: 1
		Black	Upper TB 1: 2
		Brown	Upper TB 1: 3
		Red	Upper TB 1: 4
		Yellow	Upper TB 1: 5
		Green	Upper TB 1: 6
		White	Upper TB 1: 7

<b>LM Encoder Motor to Term</b>			
Linear Motor	Black	Grey	Upper TB 1: 13
		Black	Upper TB 1: 14
		Brown	Upper TB 1: 15
		Red	Upper TB 1: 16
		Yellow	Upper TB 1: 17
		Green	Upper TB 1: 18
		White	Upper TB 1: 19

<b>LM Term Jumper 41 47</b>			
LM TB: 41	Black	Black	LM TB: 47

<b>LM Term Jumper 18 46</b>			
LM TB: 18	Black	Black	LM TB: 46

<b>LM Term Jumper 16 18</b>			
LM TB: 16	Black	Black	LM TB: 18



Linear Motor  
Main Power and Encoder

## Rotary Motor: Main Power and Encoder

110V Power			
110V Outlet	Black	Black	Power Supply Plug
		White	
		Green	

RM BM Power			
RM Power Supply: 1	Red/Black	Red	RM BM: Vcc IN +
RM Power Supply: 4		Black	RM BM: GND

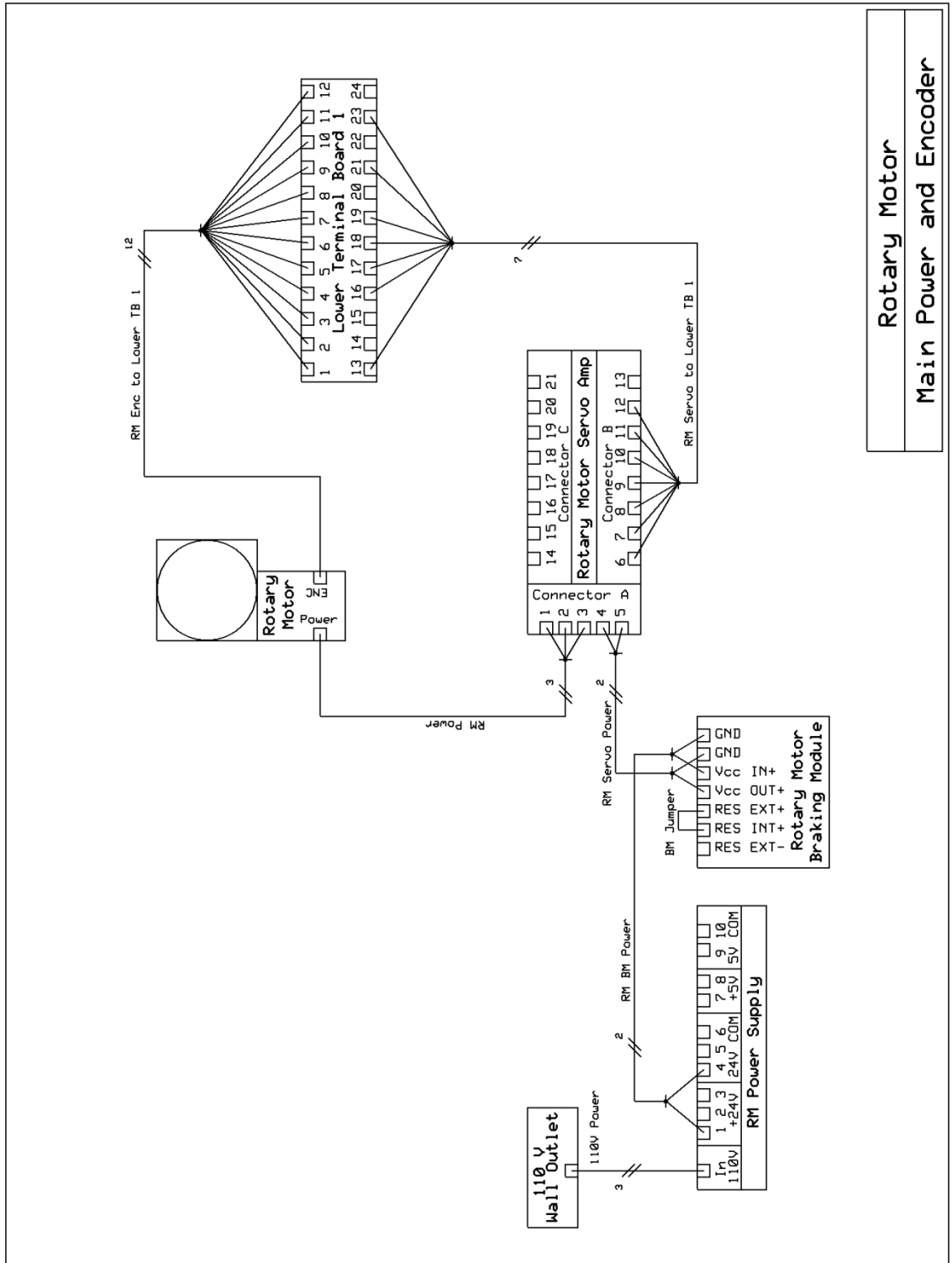
BM Jumper			
RM BM: RES INT+	Grey	Grey	RM BM: RES EXT+

RM Servo Power			
RM BM: Vcc OUT+	Red/Black	Red	RM Servo: 4
RM BM: GND		Black	RM Servo: 5

RM Power			
Rotary Motor: 7 Pin d-Sub	Green	Black 1	RM Servo: 1
		Black 2	RM Servo: 2
		Black 3	RM Servo: 3

RM Enc to Lower TB 1			
Rotary Motor: 15 Pin d-Sub	Red/Grey	Red	Lower TB 1: 1
		Grey 1	Lower TB 1: 2
		Grey 2	Lower TB 1: 3
		Grey 3	Lower TB 1: 4
		Grey 4	Lower TB 1: 5
		Grey 5	Lower TB 1: 6
		Grey 6	Lower TB 1: 7
		Grey 7	Lower TB 1: 8
		Grey 8	Lower TB 1: 9
		Grey 9	Lower TB 1: 10
		Grey 10	Lower TB 1: 11
		Grey 11	Lower TB 1: 12
		Grey 12	NC
Grey 13	NC		

RM Servo to Lower TB 1			
RM Servo: 6	Grey	Green	Lower TB 1: 13
RM Servo: 7		Blue	Lower TB 1: 23
RM Servo: 8		White/Blue	Lower TB 1: 17
RM Servo: 9		Brown	Lower TB 1: 19
RM Servo: 10		White/Orange	Lower TB 1: 18
RM Servo: 11		Orange	Lower TB 1: 16
RM Servo: 12		White/Green	Lower TB 1: 21
NC		White/Brown	NC



Rotary Motor  
Main Power and Encoder

## System: Servo On and Emergency Stop

<b>LM Servo On</b>			
RM Power Supply: 2	Red/Black	Red	LM TB: 20
RM Power Supply: 5		Black	LM TB: 41

<b>LM Control</b>			
CB LM Switch: 1	Grey	Green	LM TB: 15
CB LM Switch: 4		Black	LM TB: 42
CB Emg Stop: 11		Red	LM TB: 46

<b>LM CB Jumper</b>			
CB LM Switch: 4	Black	Black	CD Emg Stop: 12

<b>RM CB Jumper</b>			
CB RM Switch: 1	Black	Black	CB Emg Stop: 22

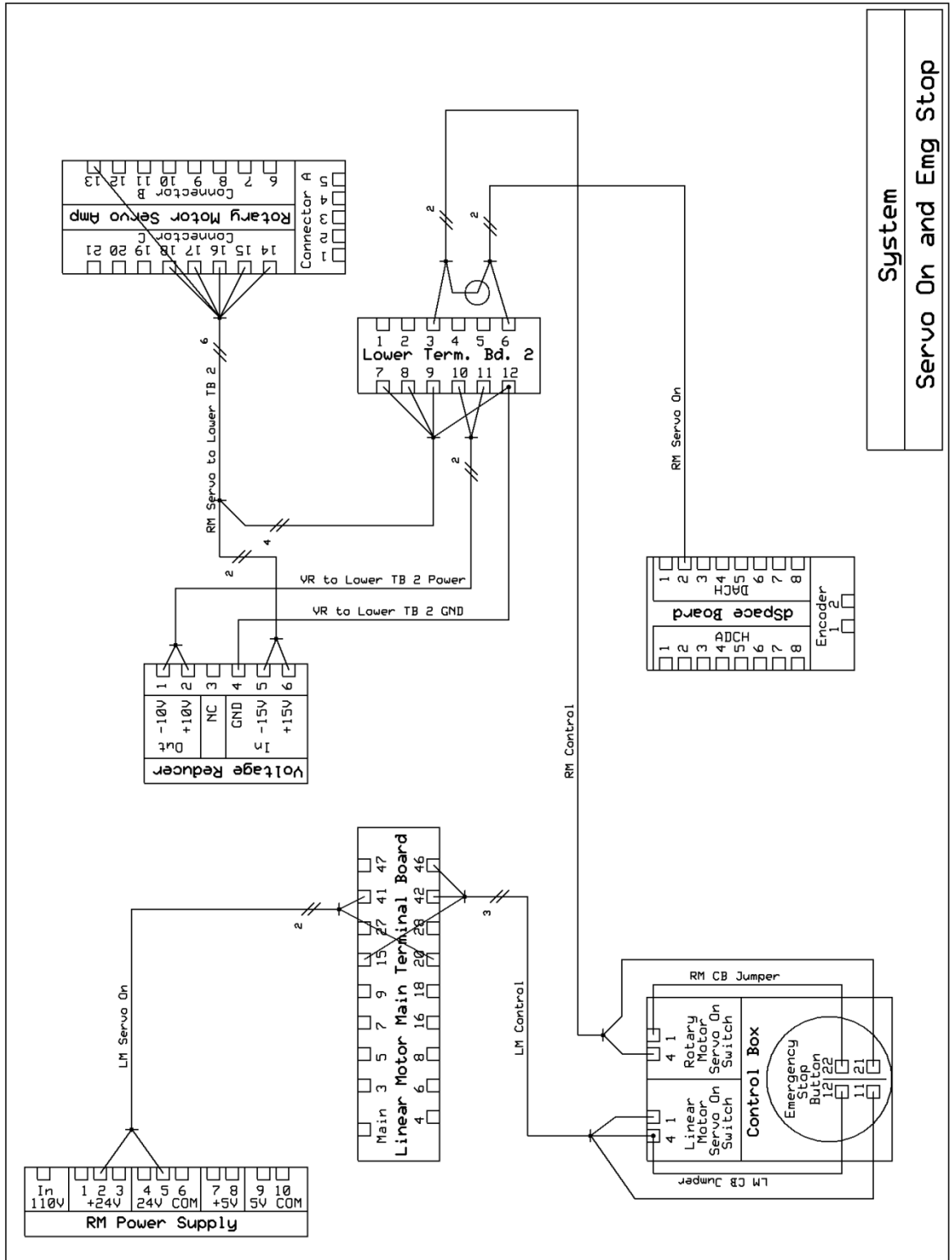
<b>RM Control</b>			
CB RM Switch: 4	Red/Black	Red	Twist Connected with: White from RM Servo On
CB Emg Stop: 21		Black	Lower TB 2: 3

<b>RM Servo On</b>			
dSpace: DACH 2	Black	White	Twist Connected with: Red from RM Control
		Bare	Lower TB 2: 6

<b>RM Servo to Lower TB 2</b>			
Lower TB 2: 7	Grey	White/Orange	RM Servo: 17
Lower TB 2: 8		Orange	RM Servo: 18
Lower TB 2: 9		White/Green	RM Servo: 13
Lower TB 2: 12		Brown	RM Servo: 15
VR: IN 5		White/Blue	RM Servo: 16
VR: IN 6		Blue	RM Servo: 14
NC		Green	NC
NC		White/Brown	NC

<b>VR to Lower TB 2 GND</b>			
VR: IN 4	Brown	Brown	Lower TB 2: 12

<b>VR to Lower TB 2 Power</b>			
VR: OUT 1	Blue/ (White/Blue)	White/Blue	Lower TB 2: 10
VR: OUT 2		Blue	Lower TB 2: 11



**System**  
Servo On and Emg Stop

## System: Limit Switches

<b>RM Limit</b>			
RM Limit: NO	Red/Black	Black	Upper TB 1: 21
RM Limit: COM		Red	Lower TB 2: 4

<b>RM Limit to dSpace</b>			
Upper TB 1: 9	Black	White	dSpace: ADCH 5
Upper TB 1: 10		Bare	

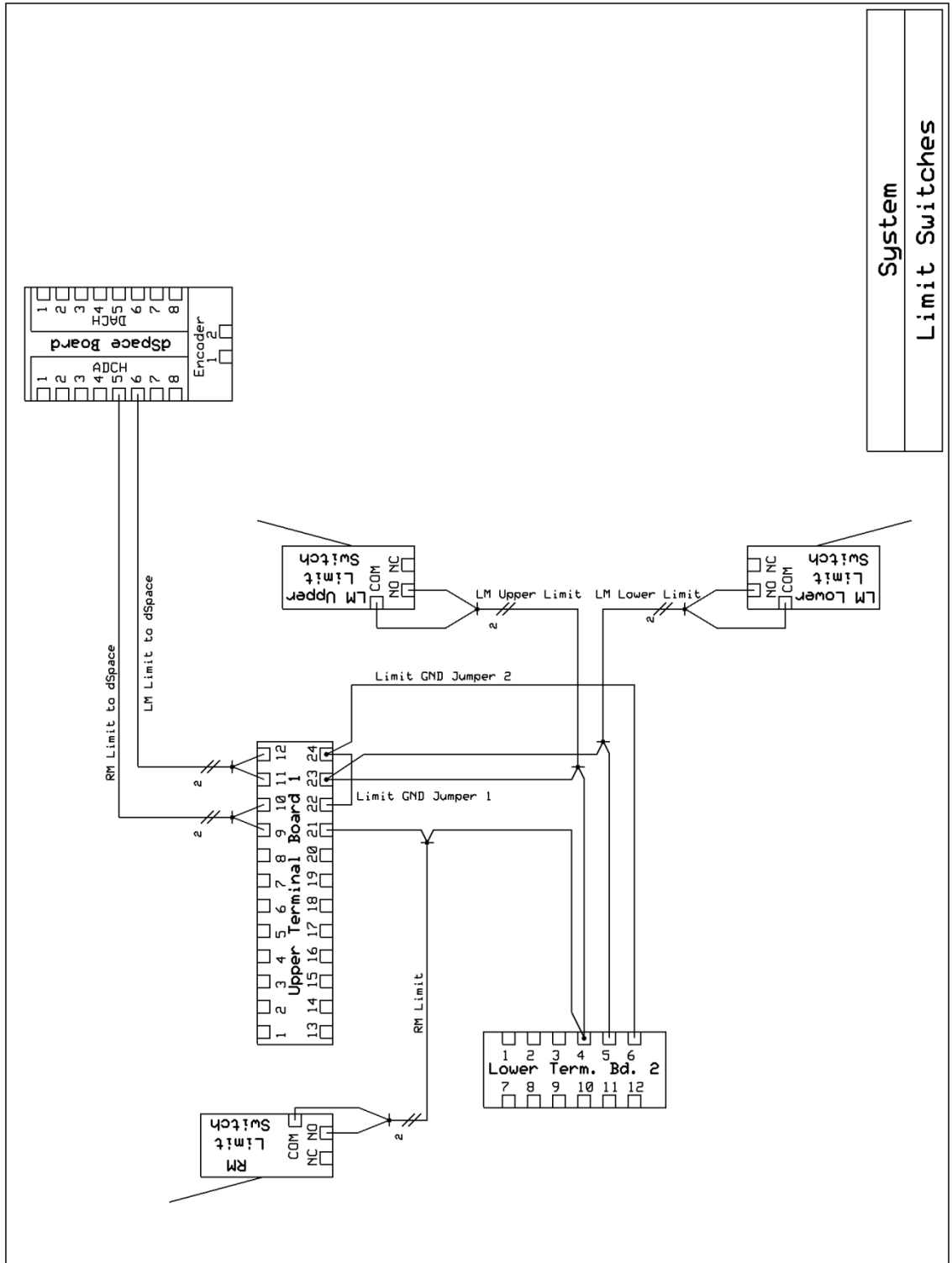
<b>LM Limit to dSpace</b>			
Upper TB 1: 11	Black	White	dSpace: ADCH 6
Upper TB 1: 12		Bare	

<b>Limit GND Jumper 1</b>			
Upper TB 1: 22	Black	Black	Upper TB 1: 24

<b>Limit GND Jumper 2</b>			
Lower TB 2: 6	Black	Black	Upper TB 1: 24

<b>LM Upper Limit</b>			
Lower TB 2: 4	Red/Black	Red	LM Upper Limit: COM
Upper TB 1: 23		Black	LM Upper Limit: NO

<b>LM Lower Limit</b>			
Lower TB 2: 5	Red/Black	Red	LM Lower Limit: COM
Upper TB 1: 23		Black	LM Lower Limit: NO



System  
Limit Switches

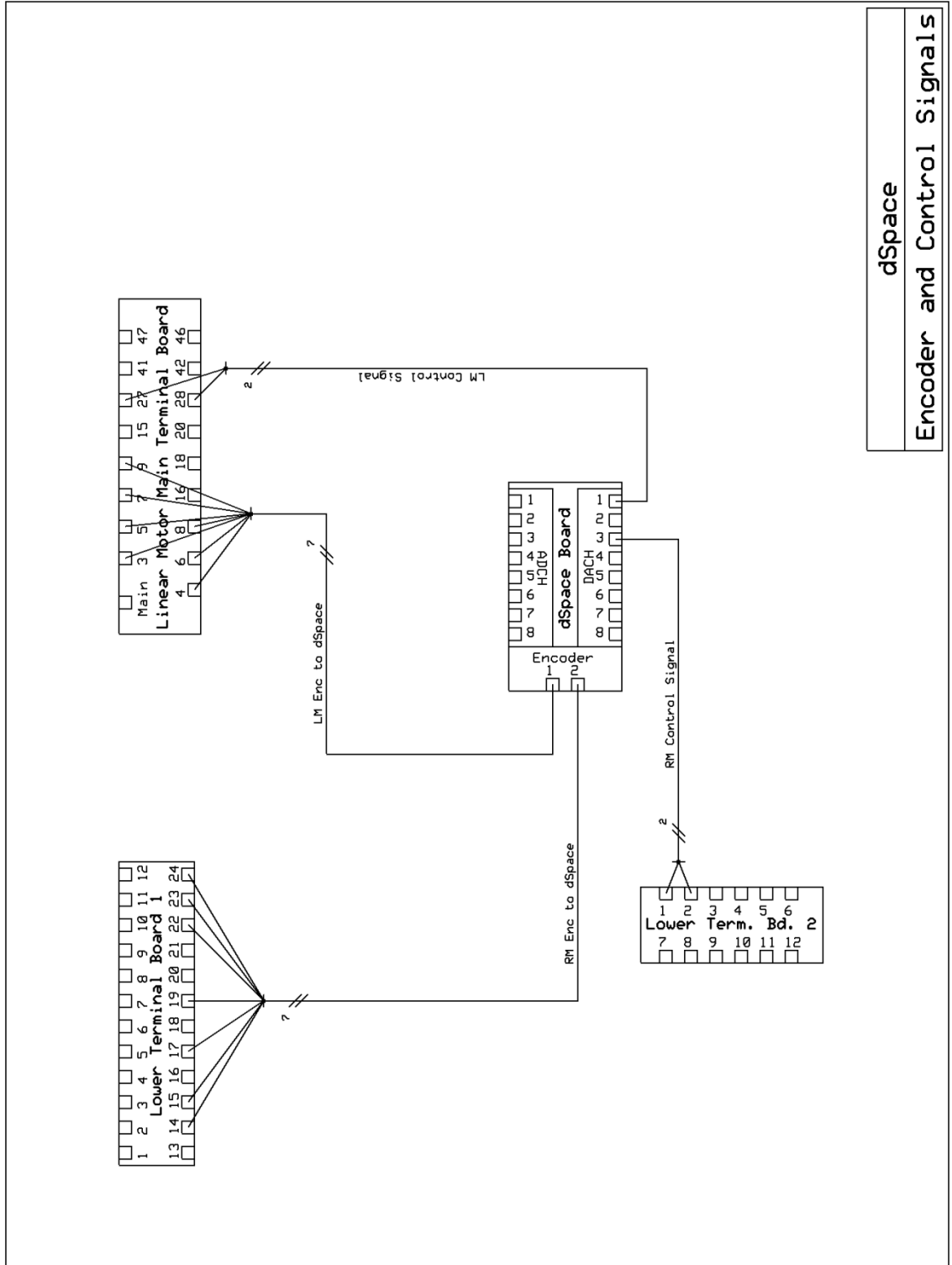
## dSpace: Encoder and Control Signals

<b>RM Enc to dSpace</b>			
Lower TB 1: 14	Grey	Green	dSpace: Encoder 2
Lower TB 1: 15		White/Green	
Lower TB 1: 17		Blue	
Lower TB 1: 19		Brown	
Lower TB 1: 22		White/Brown	
Lower TB 1: 23		Orange	
Lower TB 1: 14		White/Blue	
NC		White/Orange	NC

<b>LM Enc to dSpace</b>			
LM TB: 3	Grey	Brown	dSpace: Encoder 1
LM TB: 4		Orange	
LM TB: 5		White/Orange	
LM TB: 6		Green	
LM TB: 7		White/Green	
LM TB: 8		Blue	
LM TB: 9		White/Blue	
NC			

<b>RM Control Signal</b>			
Lower TB 2: 1	Black	White	dSpace: DACH 3
Lower TB 2: 2		Bare	

<b>LM Control Signal</b>			
dSpace: DACH 1	Black	White	LM TB: 27
		Bare	LM TB: 28



dSpace  
Encoder and Control Signals

## dSpace: Remaining Signals

<b>Main Prosthesis 1</b>			
Prosthesis QD (Fem): 1	Grey	Red	Upper TB 2: 4
Prosthesis QD (Fem): 2		Blue	Upper TB 2: 3
Prosthesis QD (Fem): 3		Green	Upper TB 2: 5
Prosthesis QD (Fem): 4		Yellow	Upper TB 2: 6
Prosthesis QD (Fem): 5		Black	Upper TB 2: 2
Prosthesis QD (Fem): 6		Grey	Upper TB 2: 1
Prosthesis QD (Fem): 7		Orange	Twist Connected with: Knee Angle to dSpace White
NC		Brown	NC

<b>Main Prosthesis 2</b>			
Prosthesis QD (Male): 1	Grey	Yellow	LC QD (Fem): 2
Prosthesis QD (Male): 2		Green	LC QD (Fem): 3
Prosthesis QD (Male): 3		Blue	LC QD (Fem): 4
Prosthesis QD (Male): 4		Red	LC QD (Fem): 1
Prosthesis QD (Male): 6		Orange	Knee Angle Sensor: 2
Prosthesis QD (Male): 7		Grey	Knee Angle Sensor: 3
Prosthesis QD (Male): 8		Black	Knee Angle Sensor: 1
NC			Brown

<b>Knee Angle Power</b>			
RM Power Supply: 7	Red/Black	Red	Upper TB 2: 8
RM Power Supply: 9		Black	Upper TB 2: 7

<b>LC Power</b>			
Upper TB 2: 9	Red/Black	Black	LC Power Supply: -
Upper TB 2: 10		Red	LC Power Supply: +

<b>Knee Angle to dSpace</b>			
Upper TB 2: 7	Black	Bare	dSpace: ADCH 7
Twist Connected with: Knee Angle Orange		Red	

<b>LC to BW</b>			
Upper TB 2: 11	Black	Bare	Brickwall Filter: In
Upper TB 2: 12		White	

<b>MP to LC</b>			
LC QD (Fem): 3	Black	Black	Load Cell: D
LC QD (Fem): 4		Green	Load Cell: B
LC QD (Fem): 5		White	Load Cell: C
LC QD (Fem): 6		Red	Load Cell: A
NC		Orange	Load Cell: E
NC		Blue	Load Cell: F
NC			

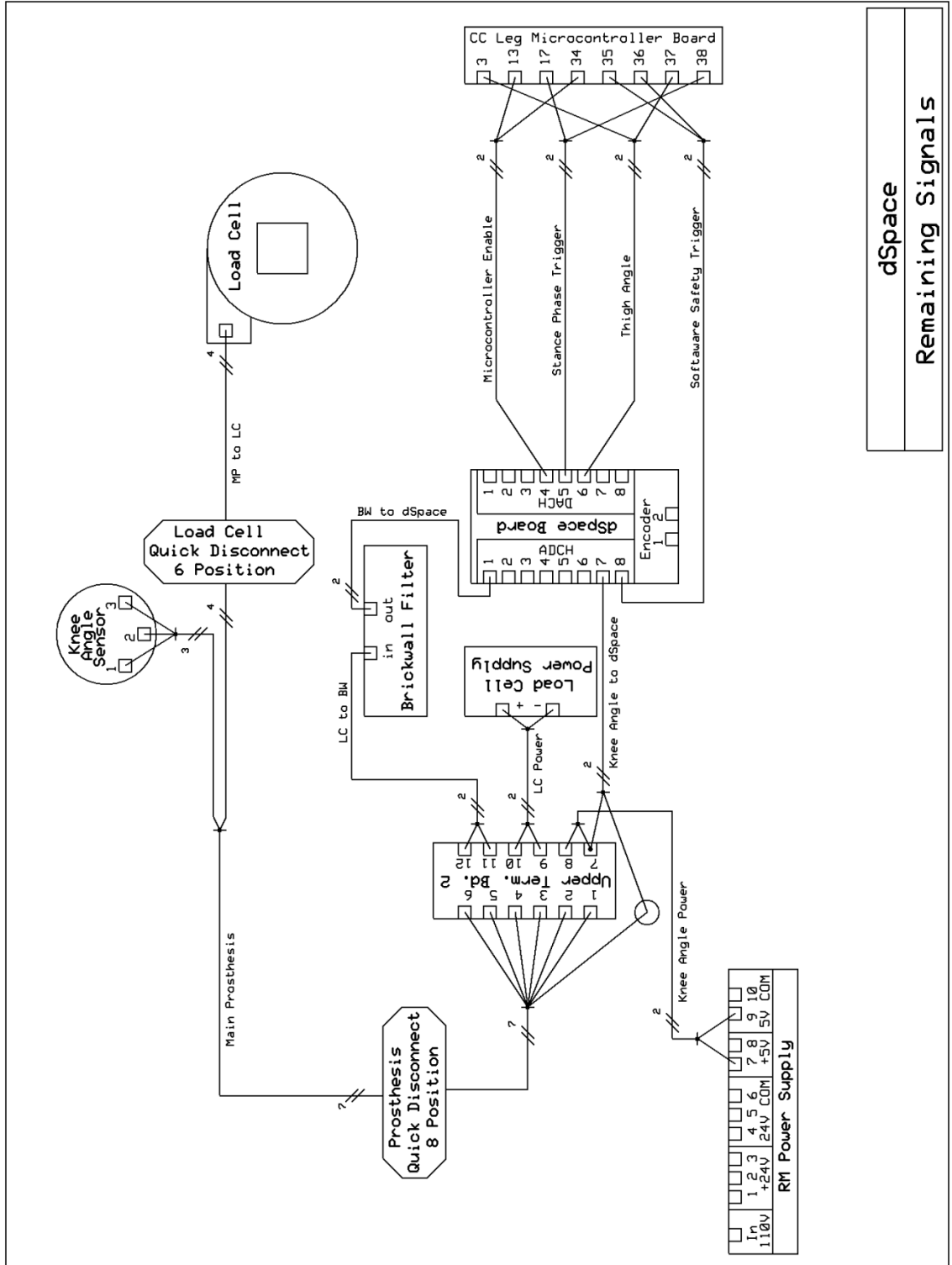
<b>BW to dSpace</b>			
Brickwall Filter: Out	Black	White	dSpace: ADCH 1
		Bare	

<b>Microcontroller Enable</b>			
dSpace: DACH 4	Purple/Black	Purple	MC Board: 13
		Black	MC Board: 34

<b>Stance Phase Trigger</b>			
dSpace: DACH 5	White/Grey	White	MC Board: 17
		Grey	MC Board: 38

<b>Thigh Angle</b>			
dSpace: DACH 6	Green/Blue	Green	MC Board: 37
		Blue	MC Board: 3

<b>Software Safety Trigger</b>			
dSpace:	Yellow/Brown	Yellow	MC Board: 36
		Brown	MC Board: 35



dSpace  
Remaining Signals



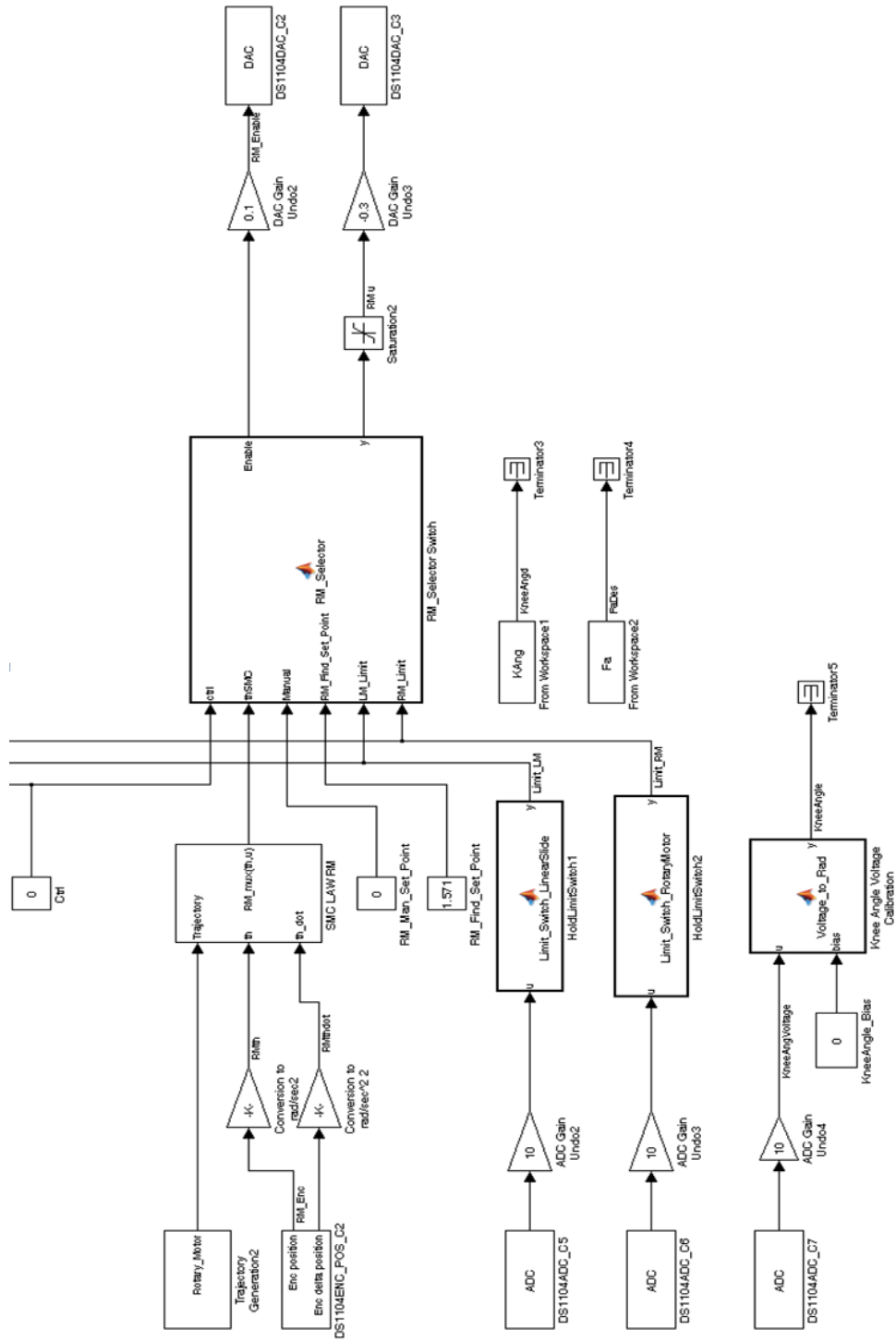
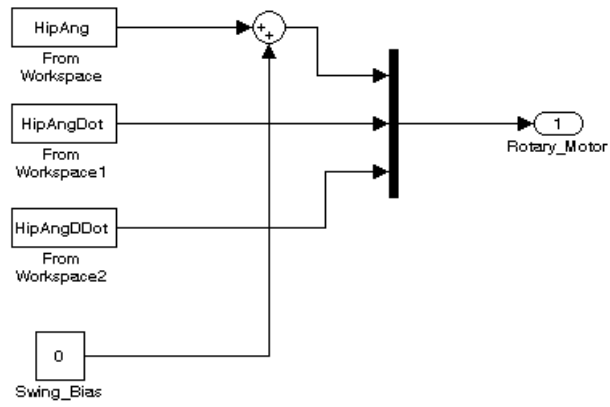


Figure 31: Hip robot Simulink diagram (part 2/2).





**Figure 33: "Trajectory Generation 2" hip robot Simulink Subsystem.**

## APPENDIX C: dSpace

Here we document the HR dSpace-HMI. The following are the instruments we use in dSpace. Following the instruments are screenshots of the actual HR dSpace-HMI.

### Instruments

The slider, Figure 15, allows us to adjust a variable in Simulink by moving the slider. This is especially useful when tuning a controller where slight adjustments are necessary. We also use the slider to manually adjust the position of the drive-stages.

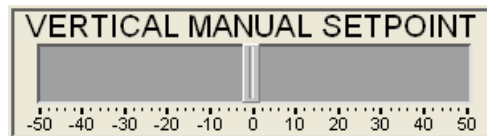


Figure 34: Slider from dSpace.

The input box, Figure 16, allows us to overwrite the value of a variable by inputting its new value with the keyboard. We use this to set the initial starting positions of the drive stages.

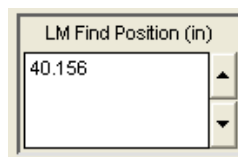


Figure 35: Input box from dSpace.

The plotter, Figure 17, is a graphical display of one or more signals over time. For our purposes we graph the encoder position feedback versus the desired set point so that we can monitor our controller's tracking.

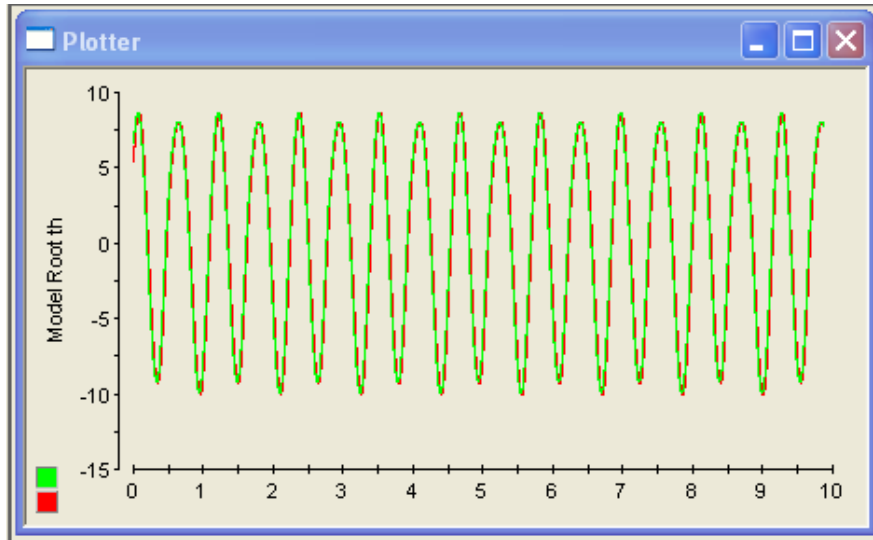


Figure 36: Plotter in dSpace.

The display, Figure 18, exhibits the value of a variable.



Figure 37: Display from dSpace.

Lastly the selector button, Figure 190, allows us to change the value of a variable based on set values. For our purposes the selector button shown in Figure 10 changes the operation mode of the robot. We have four different modes of operation: manual control of position, follow set point using SMC, find limit (for establishing absolute position), and find position, which establishes the starting point of the drive stages.

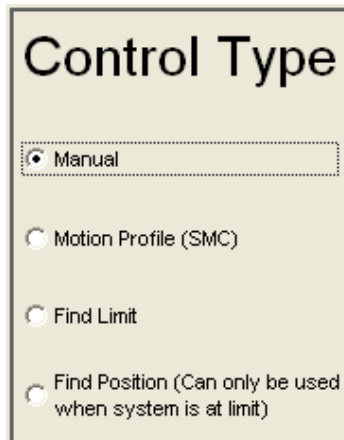


Figure 38: Selector button from dSpace.

# dSpace-HMI



Figure 39: dSpace HMI system (part 1/3).

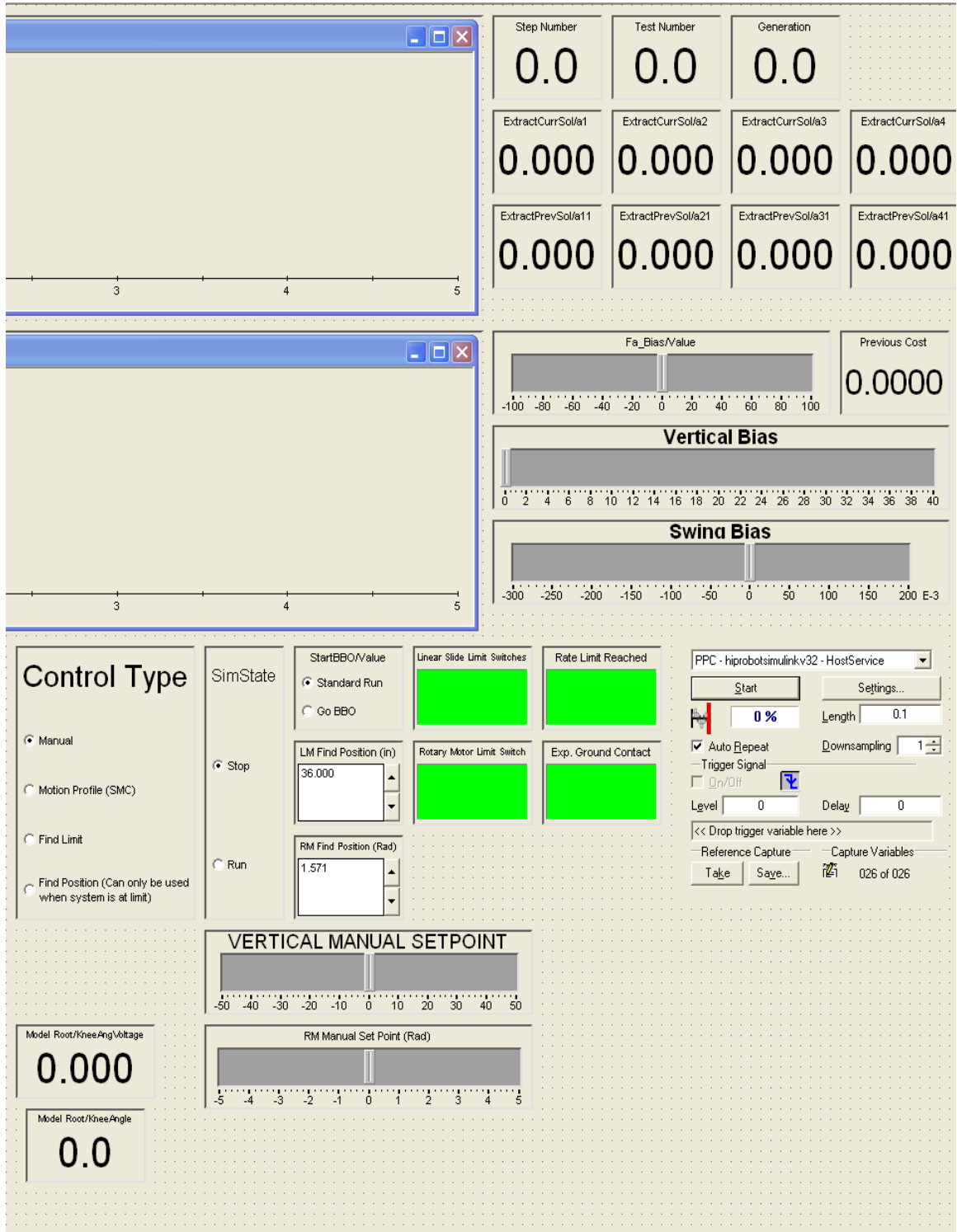


Figure 40: dSpace HMI system (part 2/3).

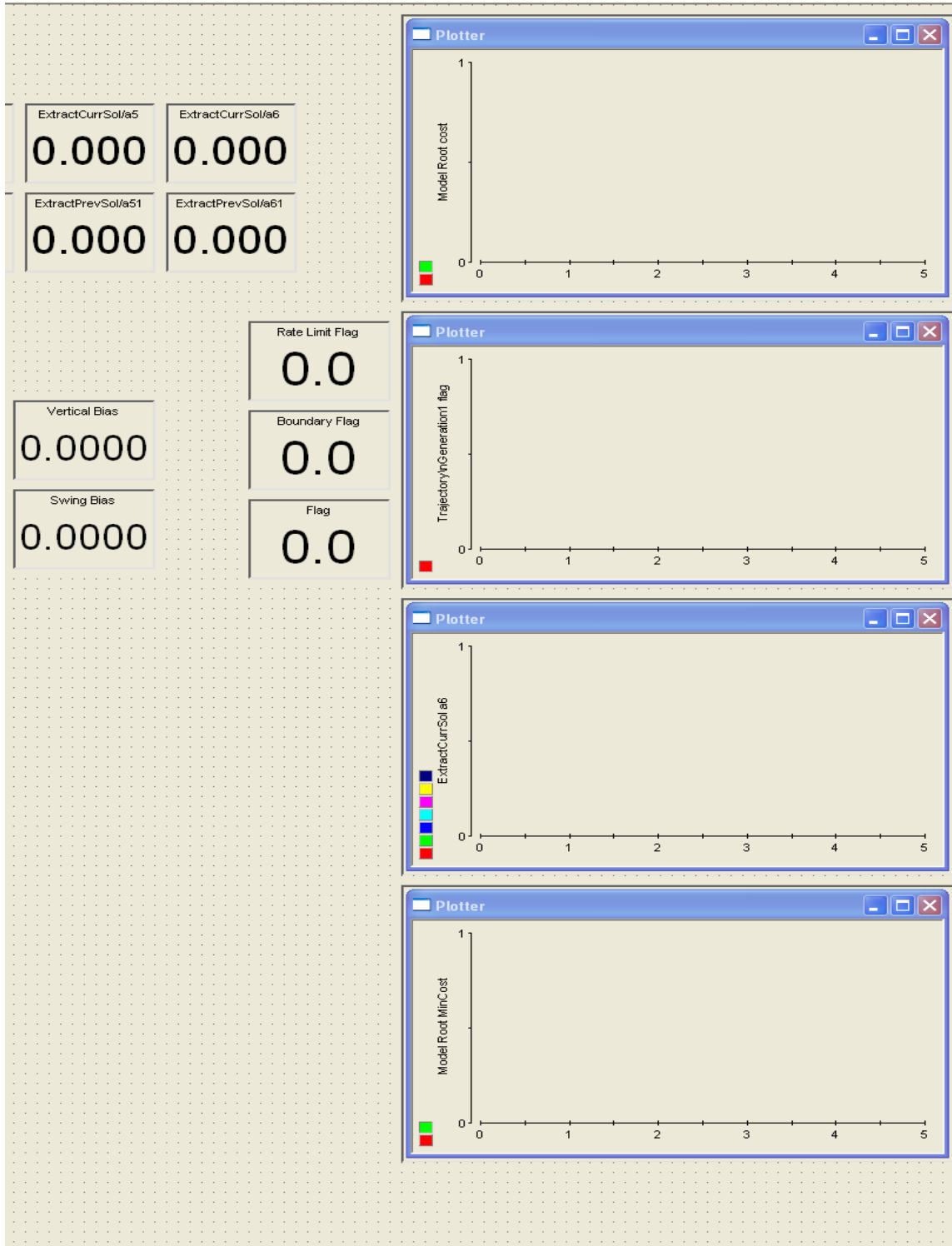


Figure 41: dSpace HMI system (part 3/3).